Two CTCF motifs impede cohesin-mediated DNA loop extrusion

Barth, Roman; Janissen, Richard; Muras, Laura; van der Torre, Jaco; Litos, Gabriele; van der Sluis, Eli; van den Berg, Ashmiani; Davidson, Iain F.; Peters, Jan Michael; Dekker, Cees

DOI
10.1016/j.molcel.2025.11.001

Publication date
2025

Document Version
Final published version

Published in
Molecular cell

Citation (APA)
Barth, R., Janissen, R., Muras, L., van der Torre, J., Litos, G., van der Sluis, E., van den Berg, A., Davidson, I. F., Peters, J. M., & Dekker, C. (2025). Two CTCF motifs impede cohesin-mediated DNA loop extrusion. *Molecular cell*, *85*(23), 4304-4317.e9. https://doi.org/10.1016/j.molcel.2025.11.001

Molecular Cell

Article

Two CTCF motifs impede cohesin-mediated DNA loop extrusion

Graphical abstract

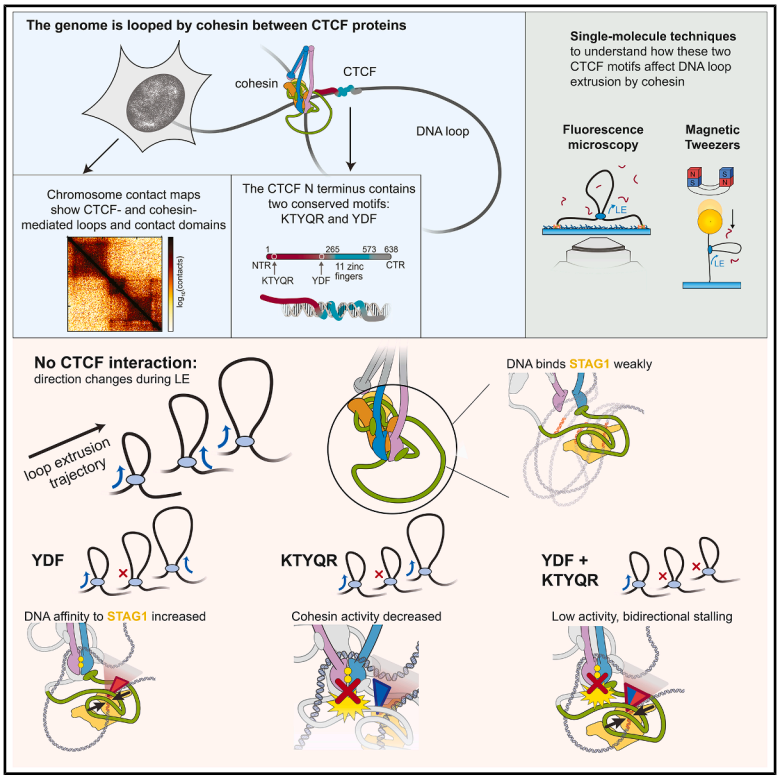

Highlights

- Human cohesin's DNA loop extrusion is stalled by CTCF's N terminus, not its C terminus
- The YDF and KTYQR N-terminal motifs interact with cohesin and stall loop extrusion
- YDF converts bidirectional extrusion to unidirectional by modulating STAG1's DNA affinity
- YDF and KTYQR together largely resemble the effect of the NTR

Authors

Roman Barth, Richard Janissen, Laura Muras, ..., Iain F. Davidson, Jan-Michael Peters, Cees Dekker

Correspondence

c.dekker@tudelft.nl

In brief

Cohesin extrudes DNA into loops until stalled by CTCF, but how CTCF achieves this is unclear. Barth et al. identified two CTCF motifs, YDF and KTYQR, which distinctly hinder DNA loop extrusion: YDF converts bidirectional cohesin into a unidirectional extruder, while KTYQR blocks extrusion, revealing how CTCF positions cohesin genome wide.

Barth et al., 2025, Molecular Cell *85*, 4304–4317
December 4, 2025
https://doi.org/10.1016/j.molcel.2025.11.001

CellPress

CellPress

Molecular Cell

Article

Two CTCF motifs impede cohesin-mediated DNA loop extrusion

Roman Barth,[1,3,4] Richard Janissen,[1,3,5] Laura Muras,[1,3,6] Jaco van der Torre,[1] Gabriele Litos,[2] Eli van der Sluis,[1] Ashmiani van den Berg,[1] Iain F. Davidson,[2] Jan-Michael Peters,[2] and Cees Dekker[1,7,*]

[1]Department of Bionanoscience, Kavli Institute of Nanoscience Delft, Delft University of Technology, Delft 2629HZ, the Netherlands
[2]Research Institute of Molecular Pathology, Vienna BioCenter Vienna 1030, Austria
[3]These authors contributed equally
[4]Present address: Institute of Protein Design, Department of Biochemistry, Seattle, WA, USA
[5]Present address: Institute of Bioengineering, Deggendorf Institute of Technology, Oberschneiding 94363, Germany
[6]Present address: Department of Cell and Molecular Biology, Science for Life Laboratory, Uppsala University, 75105 Uppsala, Sweden
[7]Lead contact
*Correspondence: c.dekker@tudelft.nl
https://doi.org/10.1016/j.molcel.2025.11.001

SUMMARY

Human cohesin extrudes DNA into loops and is positioned along the genome by stalling at the human CCCTC-binding factor (CTCF) upon encountering its N-terminal region (NTR). The mechanism underlying this stalling, however, is unresolved. Using single-molecule assays that monitor DNA loop extrusion (LE) in the presence of NTR fragments, we identify two amino acid motifs, YDF and KTYQR, which hinder LE. KTYQR is found to completely block LE activity, while YDF hinders cohesin from completing LE step cycles and converts cohesin into a unidirectional extruder by strengthening the affinity of STAG1 to DNA. We thus identify two distinct NTR motifs that stall LE via different yet synergistic mechanisms, highlighting the multifaceted ways employed by CTCF to modulate LE to shape and regulate genomes.

INTRODUCTION

The spatial organization of the genome is crucial for processes like transcription, replication, and DNA repair.[1,2] Central to chromosomal architecture are DNA loops, which are progressively extruded by the structural maintenance of chromosomes (SMC) ATPases condensin I/II, cohesin, and SMC5/6 in humans.[3–10] Cohesin (Figure 1A) forms DNA loops in interphase[11–14] and extrudes DNA asymmetrically while frequently switching direction,[3,15] forming large topologically associated domains (TADs) whose boundaries are demarcated by CCCTC-binding factor (CTCF).[12,14,16–20] DNA loops extruded by cohesin and associated with CTCF-positioned loops and TADs are implicated in a range of biological processes. For instance, the regulation of specific genes depends on the proper positioning of cohesin, CTCF, and TADs.[21,22] Especially during development, (dis)activating specific gene-regulatory circuits appears to depend critically on cohesin-mediated loop extrusion (LE).[22–25] Beyond transcription, DNA LE by cohesin also impacts replication,[26,27] possibly by interacting with parts of the replisome.[28] CTCF positions DNA loops at TAD boundaries by stalling cohesin, a tightly regulated process that is directional: the majority of CTCF binding sites are oriented such that CTCF's N-terminal region (NTR) points toward the TAD interior,[14,29–33] indicating that the NTR mediates loop positioning. Indeed, previous single-molecule *in vitro* experiments showed that CTCF stalls DNA LE by cohesin, particularly when approached from its NTR.[34,35] The interaction depends strongly, but not exclusively, on a YDF motif[34,36–40] in the NTR (residues 226–228 of CTCF; Figure 1A) that binds to a "conserved essential surface" (CES) formed by the kleisin and STAG1/2 cohesin subunits.[41–47] This motif is shared with other proteins that have been shown to interact with cohesin *in vivo* and *in vitro*.[28] Mutations in the YDF motif reduce CTCF-anchored loops[41] but have less impact on cohesin enrichment at CTCF sites,[41] indicating that cohesin-CTCF co-localization alone is insufficient to form these loops[37,41,48–50] or that the YDF motif is not the only mechanism by which cohesin stalls at CTCF sites. The underlying mechanism of how CTCF inhibits cohesin-mediated LE has been coined a "mechanistic mystery."[48] Indeed, it remains an important unresolved question how CTCF regulates cohesin-driven LE and hence impacts critical cellular processes such as protocadherin isoform diversity,[23] diseases such as cohesinopathies (e.g., Cornelia de Lange syndrome[51] and Roberts syndrome[52]) or cancer[53] (e.g., acute myeloid leukemia and myelodysplastic syndromes), and in V(D)J recombination.[54,55]

With the aim of understanding the molecular mechanisms by which CTCF affects cohesin-mediated LE, we dissected the

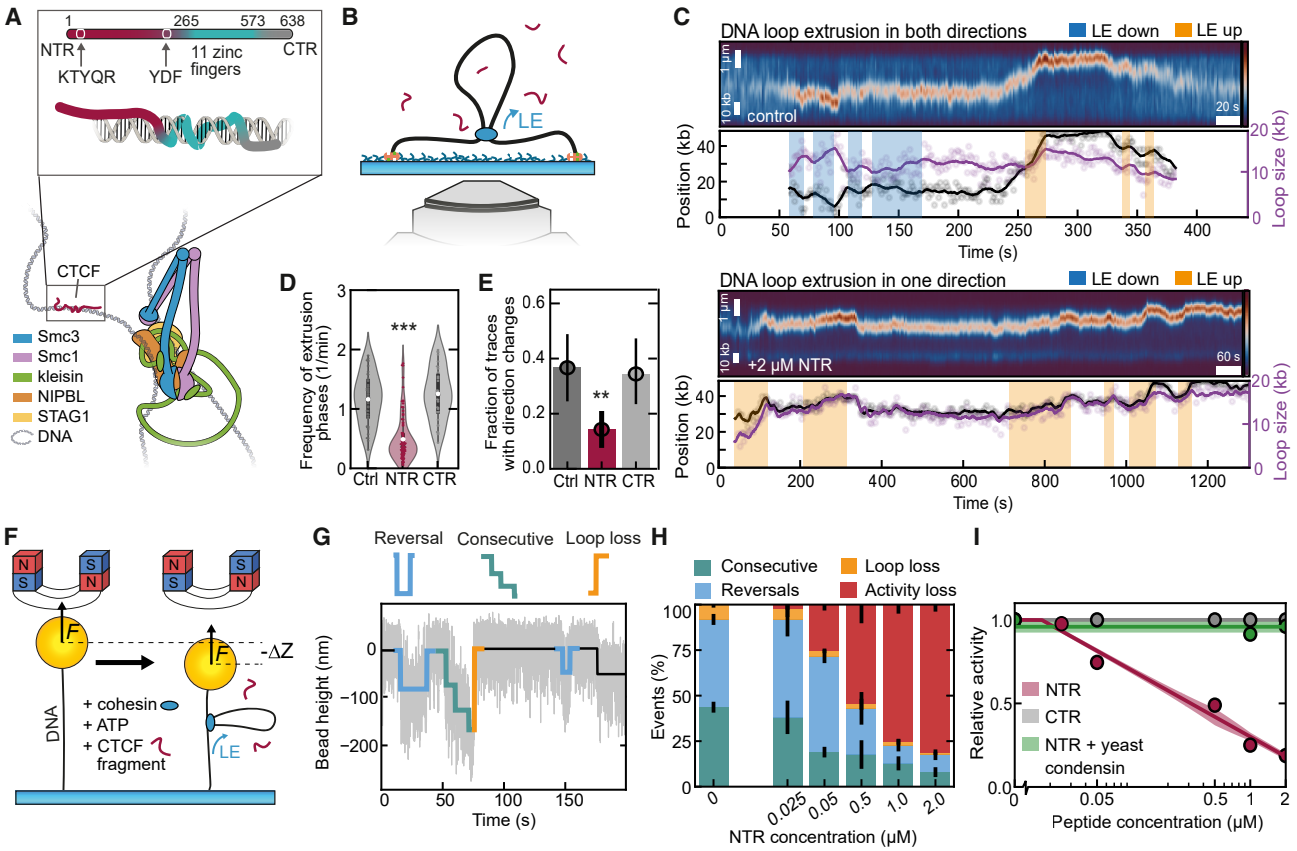

Figure 1. The NTR of CTCF impedes cohesin-mediated LE

(A) Illustration of a DNA-bound human cohesin complex (bottom; based on PDB: 7W1M[27]) and CTCF (top). CTCF shows the N-terminal region (NTR; red) and C-terminal region (CTR; gray) of CTCF, separated by 11 zinc fingers (cyan) that bind to DNA.

(B) Fluorescence visualization assay to observe cohesin-mediated LE on individual, surface-tethered DNA molecules.

(C) Example kymograph of LE that consistently extrudes in both directions (lower) or toward one direction (upper). Segmented extrusion phases (STAR Methods and Ryu et al.[56]) are shaded yellow for extrusion upward and blue for extrusion downward. Loop position (black) and size (purple) are shown below. Solid lines depict smoothed data (STAR Methods).

(D) Violin plot of the frequency with which extrusion phases occur in the absence (control) or the presence of 2 μM CTCF NTR or CTR. White dots denote the mean, the box shows the quartiles of the data, and whiskers extend to 1.5 × interquartile range. Statistical significance was assessed by a Kruskal-Wallis test (***$p < 0.001$ and the Cliff's Delta statistic is $\geq$0.33). n = 45, 91, and 40 DNA molecules from left to right.

(E) Fraction of traces that show direction changes in the absence (control) or the presence of 2 μM CTCF NTR or CTR. Error bar denotes the 95% binomial confidence interval (CI). Statistical significance was assessed by a two-sided Fisher's exact test (**$p < 0.01$ and the 95% odds ratio CI does not contain 1). n = 58, 103, and 57 DNA molecules from left to right.

(F) Magnetic tweezer (MT) experimental setup used to measure individual LE steps.[26,47,49]

(G) Example MT trace and illustration of the classification of LE stepping events into reversals (blue), consecutive LE steps (green), and loop loss (orange). Raw data are shown in light gray; the black line shows the resulting fit from the step-finding algorithm (STAR Methods).

(H) Fraction of events classified as consecutive steps (green), reversals (blue), and loop loss (orange) for MT traces, with increasing concentrations of CTCF NTR. Loss in activity (red) denotes that proportionally fewer steps are observed compared with the control measurement ([NTR] = 0 μM). Error bars denote 95% binomial CIs. n = 1,097, 109, 537, 46, 75, and 77 steps from 193, 19, 114, 16, 51, and 103 tethers, respectively, for increasing CTCF NTR concentration.

(I) The relative LE activity of cohesin, compared with the corresponding control ([peptide] = 0 μM), for increasing concentrations of CTCF NTR, CTR, and NTR in combination with yeast condensin. The data correspond to the inverse of the red bar height of (H) and Figures S1K and S1L, respectively. Fits serve as a guide for the eye (STAR Methods). Lines denote the fit and the shaded error bars denote the mean and interpolated SD of the individual data points.

CTCF NTR into fragments and investigated their effects on LE with single-molecule and bulk biochemical methods. We found that the presence of the complete NTR reduces the frequency of active LE phases and causes cohesin to mainly extrude loops from one side only. The latter effect is attributed to an increase in STAG1's DNA affinity induced by the YDF motif, preventing DNA strand exchange and direction switching. Although the YDF motif reduces cohesin's ATPase activity as well as hinders cohesin from taking consecutive LE steps, its effect on cohesin is weaker than that of the full NTR. We identified and studied a second motif, KTYQR (residues 23–27 of CTCF[49]), which independently reduces cohesin's ATPase activity and blocks cohesin-mediated LE. These findings clarify how CTCF influences cohesin's LE dynamics and shapes genomes.

RESULTS

The NTR of CTCF impedes cohesin-mediated DNA LE

To probe cohesin's LE behavior in response to the CTCF NTR and C-terminal region (CTR) (Figure S1A) on the single-molecule level, we added purified 100 pM human cohesin^{STAG1} (henceforth "cohesin") and 250 pM NIPBL-Mau2 to surface-tethered λ-DNA[4] (Figure 1B; STAR Methods), and measured its LE activity in the presence of a buffer containing fragments of CTCF. This approach probes LE by cohesin in a buffer with CTCF fragments in solution, providing a high-throughput assay that probes the essential interactions between cohesin and CTCF, which in cells are both bound to DNA. Because short amino acid sequences often bind to their interaction partners with lower affinity as isolated peptides than in the context of folded proteins, we used CTCF peptides in large excess over cohesin and controlled their binding specificities by using scrambled and mutated peptides. The LE dynamics in kymographs (Figure 1C; STAR Methods) show that, as reported before,[15] cohesin alternated between active extrusion phases and diffusion/slipping phases, with stochastic direction changes (Figure 1C) occurring upon exchange of the NIPBL subunit.[15] The following terminology is used to describe cohesin's directionality: cohesin is, like all SMCs,[15] an asymmetric loop extruder, i.e., it always extrudes DNA only from one side at a time into the loop. Furthermore, it is a bidirectional extruder, as it undergoes subsequent phases of asymmetric extrusion (i.e., extruding DNA for a while "from the left" and then for a while "from the right," etc.) that are interrupted by pauses during which the side from which the DNA is incorporated into the loop switches direction (Figure 1C, upper). This contrasts a unidirectional extruder like yeast condensin, which undergoes subsequent phases of asymmetric extrusion that always occur in the same direction (Figure 1C, lower).[15]

In the presence of 2 μM NTR (residues 2–259) in this single-molecule visualization assay, the frequency of active extrusion phases decreased ~3-fold compared with conditions without NTR (Figure 1D). Notably, the extrusion rate during active phases remained unchanged (Figure S1B), suggesting that the NTR particularly hinders cohesin to initiate LE phases. Bidirectional extrusion (i.e., cohesin sequentially reels in DNA from the left and right sides during traces) decreased from 35% to 12% of cases in the presence of the NTR (Figure 1E), indicating that the NTR converts cohesin into a predominantly unidirectional extruder (consequently reeling in DNA from one side only). The CTR had no effect on LE activity or directionality.

Magnetic tweezer (MT) experiments (Figure 1F; STAR Methods), which are able to detect LE on individual DNA molecules with single-step resolution,[34,56–58] showed three distinct signatures (Figure 1G): consecutive downward steps (>1 step); single downward steps followed by upward backsteps of the same size, consistent with incomplete LE cycles ("reversals"; STAR Methods; Ryu et al.[56] and Janissen et al.[58]); and (rare) large upward steps that resolved previous downward steps ("loop loss"). Consecutive steps relate to cohesin's stepwise LE activity,[34,56,58] while we attribute reversals to incomplete LE step cycles, e.g., as a consequence of the inability to hydrolyze the ATP necessary to perform the LE step.[56,58] Current mechanistic models propose that DNA is reeled into the Smc lumen upon ATP binding, creating a downward step.[59–61] Recent molecular dynamics simulations of SMC-driven LE suggest that DNA may often slip out of the lumen,[62] constituting unsuccessful LE steps. We therefore consider reversals as failed attempts at completing the LE hydrolysis cycle (Figure S1C). We developed a step-finding algorithm that more accurately extracted steps compared with our previous method (STAR Methods; Figures S1D–S1H[63]).

In the presence of the NTR of CTCF, cohesin's LE activity decreased in a concentration-dependent manner, with fewer steps observed within our 12-min acquisition period (Figure 1H; Figures S1I and S1J), where the total activity dropped to 20% at 2 μM NTR compared with control experiments without NTR. Both consecutive steps and reversals were equally affected, maintaining a constant ratio (Figures S1M–S1O). Importantly, no dependence on CTCF was observed in similar experiments using yeast condensin (Figure 1I; Figures S1K and S1M–S1O; STAR Methods), confirming the specificity of NTR's impact on human cohesin. Similarly, addition of the CTR (Figures 1I and S1L–S1O) had no effect whatsoever. Previously, we observed that a fraction of loop-extruding cohesin molecules can be stalled by full-length DNA-bound CTCF, even when approached from its C-terminal side.[34] Note that CTCF in these experiments contained both the NTR and CTR, and we hypothesized that—despite the encounter from the C-terminal side—cohesin interacted with the CTCF's NTR in these experiments. Supporting this view, the residence time of cohesin on CTCF was indistinguishable between N-terminal and C-terminal encounters (Extended Data Fig. 8 in Davidson et al.[34]), and this interpretation quantitatively recapitulates the convergent rule observed *in vivo* (Extended Data Fig. 5 in Davidson et al.[34]). The data presented here—namely, that the CTCF CTR does not interfere with cohesin-mediated LE—further support this hypothesis and align well with multiple independent recent studies showing that the NTR, but not the CTR, interacts with cohesin.[34,35,39,41,49,64] We conclude that the CTCF NTR biases cohesin toward unidirectional extrusion (Figure 1E) and significantly reduces cohesin's LE activity in a concentration-dependent manner (Figures 1D and 1I).

The YDF motif biases cohesin toward unidirectional extrusion

The CTCF NTR contains a conserved YDF motif (residues 226–228; Figure 2A; Figure S2A) that binds the CES on cohesin's STAG1/2 subunit,[41–47] which was observed to impact TAD formation.[41] To study the role of the YDF motif in inhibiting LE by cohesin, we used a very short NTR fragment containing the YDF motif (residues 222–232; "YDF peptide") and a mutated version ("ADA peptide"; Figure 2B; Table S1). Increasing concentrations of the YDF peptide significantly reduced cohesin's ATPase activity (Figure 2C; STAR Methods) and decreased the frequency of active extrusion phases (Figure 2D) by 1.5-fold, whereas the ADA peptide had no effect on either activity. Variants of the full CTCF NTR with YDF mutations (NTR^{FDF} and NTR^{ADA}; Figure 2B; Figure S3A; Table S1) reduced the frequency of extrusion phases by 2-fold (Figure 2D) but did not affect the extrusion rate (Figure S3B). The partial inhibition of cohesin observed with the NTR^{ADA} fragment, but not with the ADA peptide, suggests

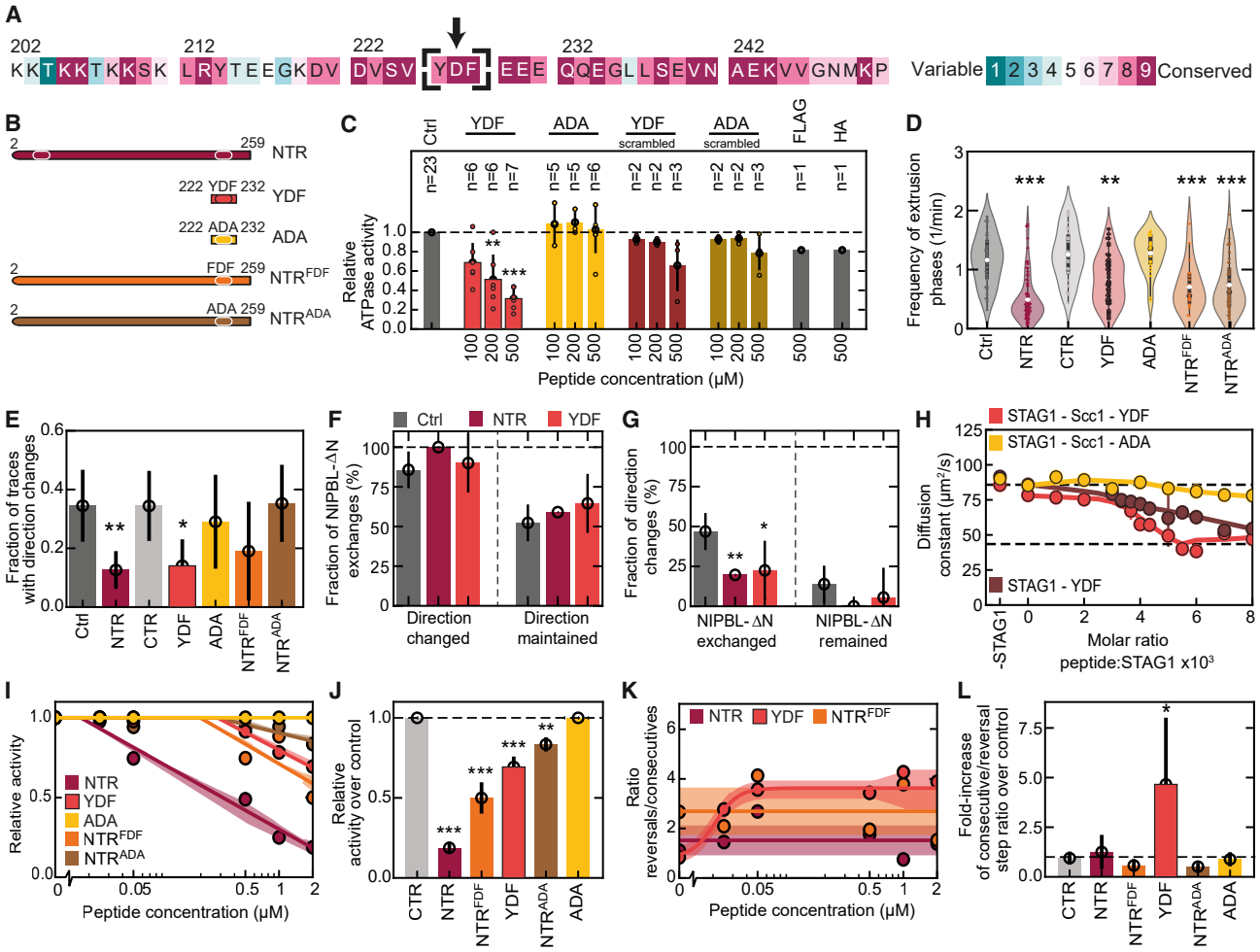

Figure 2. CTCF's YDF motif impairs cohesin's LE activity and renders LE unidirectional

(A) Conservation annotation of the human CTCF sequence surrounding the conserved YDF motif.

(B) Illustration of CTCF fragments used.

(C) Normalized ATPase activity of cohesin for various concentrations of CTCF peptide. Scrambled peptides contain the same amino acids as the non-scrambled version but in random order. Statistical significance was assessed by an ANOVA with Holm-Sidak's multiple comparison test (**$p < 0.01$; ***$p < 0.001$).

(D) Violin plot of the frequency with which extrusion phases occur in the presence of 2 μM of the indicated CTCF fragment, as in Figure 1D. $n = 45, 91, 40, 19, 49, 52$, and 25 DNA molecules from left to right.

(E) Fraction of traces that show direction changes in the absence (control) or the presence of 2 μM of the indicated CTCF fragment, as in Figure 1E. $n = 58, 103, 57, 21, 51, 57$, and 32 DNA molecules from left to right.

(F) Fraction of cohesin molecules for which NIPBL-ΔN exchanged between direction changes (left; $n = 35, 23, 27$ from left to right) and the fraction of cohesin molecules on which NIPBL-ΔN exchanged without a direction change between successive extrusion phases (right; $n = 65, 80, 64$). Error bars denote the binomial 95% CI. Statistical significance was assessed using a chi-squared test.

(G) Fraction of direction changes between successive extrusion phases during which NIPBL-ΔN exchanged ($n = 64, 65, 59$) and the fraction of direction changes between successive extrusion phases during which NIPBL-ΔN remained ($n = 36, 38, 32$). Statistical significance was assessed using a chi-squared test (*$p < 0.05$; **$p < 0.01$).

(H) Diffusion constant of DNA-STAG1$^{+/-Scc1}$- YDF and DNA-STAG1^{Scc1}-ADA complexes versus the molar ratio of peptide to STAG1 derived from a mono-exponential fit to FCS curves. Upper and lower dashed lines denote the theoretical diffusion constant of freely diffusing DNA and the DNA-STAG1^{Scc1}-YDF (or -ADA) complex, respectively. Experiments were conducted with two biological replicates and 4–9 technical replicates. Data points and error bars represent the mean ± SD of these replicates, while solid lines display a LOWESS-smoothed trend of the means.

(I) The relative LE activity of cohesin, compared with the control ([peptide] = 0 μM), versus peptide concentration as in Figure 1I. The data correspond to the inverse of the red bar height of panels Figures 1H and S3F–S3I. Fits serve as a guide for the eye (STAR Methods). Lines denote fits and the shaded error bars denote the interpolated SD of the individual data points.

(J) The relative LE activity, compared with the control, for 2 μM of the indicated peptides. Error bars denote the standard deviation from repeated experiments. Statistical significance was assessed by a one-sided Welch's t test (**$p < 0.01$; ***$p < 0.001$).

(K) The ratio of reversals to consecutive steps at increasing concentrations of the indicated peptides, from data in Figures 1H and S3F–S3I. See also Figure S3J.

(L) The ratio of reversals to consecutive steps for 2 μM of the indicated peptides, as in (J).

that additional motifs beyond YDF contribute to cohesin regulation by CTCF.

Unexpectedly, upon analyzing LE direction changes, we found that the YDF motif alone caused cohesin to extrude unidirectionally, mimicking the effect of the full NTR (Figure 2E). Although the Y226F mutation produced an intermediate (not statistically significant) effect, the Y226A/F228A mutation and the ADA peptide completely abolished the unidirectional bias. These results indicate that the YDF motif alone drives cohesin's unidirectional extrusion. Direction changes in cohesin-mediated LE have been demonstrated to require NIPBL exchange.[65] To test whether the YDF motif affects cohesin's directionality by preventing NIPBL exchange, we conducted single-molecule fluorescence experiments with an equimolar mix of NIPBL-ΔN molecules that were fluorescently labeled in two colors[15] (STAR Methods). The presence of the NTR or YDF peptides was found to not alter the residence time of NIPBL-ΔN on cohesin (Figure S3C), ruling out a slower NIPBL-ΔN exchange as the cause of unidirectional extrusion. We then correlated NIPBL presence, absence, and exchange with extrusion direction switches. Both in the absence and presence of the NTR or the YDF motif, almost all direction changes required an NIPBL-ΔN exchange (Figure 2F). Similarly, NIPBL exchanged in ∼50% of cases when the extrusion direction was maintained between successive extrusion phases (Figure 2F). In control experiments, roughly 50% of the exchanges of NIPBL-ΔN coincided with a direction switch (Figure 2G). However, in the presence of the NTR or the YDF motif, we observed that 2.5-fold fewer NIPBL-ΔN exchange events led to direction changes (Figure 2G), suggesting that the NTR and YDF motif prevent direction changes through a mechanism unrelated to NIPBL exchange dynamics.

Direction switching in SMC-mediated LE is thought to involve DNA strand exchange between the extruding and anchoring sides of the SMC complex.[6,65,66] Data showing that yeast condensin, a strictly unidirectional extruder, extrudes bidirectionally upon deletion of its anchoring Ycg1 subunit[66] led us to hypothesize that the YDF motif might inhibit DNA strand exchange by enhancing the DNA-binding affinity of STAG1. To test this, we conducted fluorescence correlation spectroscopy (FCS) experiments that measure the diffusion constant of fluorescently labeled DNA in the presence of purified STAG1, $Scc1^{251–420}$, and YDF peptide (STAR Methods). Increasing concentrations of the YDF peptide caused the DNA's diffusion constant to shift from that of freely diffusing molecules to STAG1-bound complexes, indicating an increased DNA affinity (Figure 2H; EC_{50} = 4.5 ±0.1 μM with Scc1 and 5.4 ±0.8 μM without Scc1; not measurable in the presence of ADA peptide). This effect was partially dependent on Scc1 and largely absent with the ADA peptide (Figure 2H).

MT experiments with increasing YDF peptide concentrations showed a ∼30% decrease in cohesin's LE activity at 2 μM (Figures 2I and 2J; Figures S3D–S3F). Although the number of consecutive steps decreased (Figures S3F and S3K), the fraction of reversals remained constant up to 1 μM YDF peptide (Figures S3F and S3L), resulting in an increased ratio of reversals to consecutive steps (Figures 2K and 2L). These effects were absent with the ADA peptide (Figures S2I, S2J, S2L, S3G, and S3J–S3L). YDF-mutated NTR variants (NTR^{FDF} and NTR^{ADA}) also reduced cohesin activity like the wild-type NTR but had progressively weaker effects, which were detected only at higher concentrations (Figures 2I and 2J; Figures S3H and S3I). Similar to the wild-type NTR (Figure S1M), NTR^{FDF} and NTR^{ADA} did not affect the fraction of reversals and consecutive steps (Figures 2K and 2L; Figures S3J–S3L). The reduced effect of these mutations on cohesin-mediated LE is likely due to lower binding affinity of the YDF mutations compared with the wild-type YDF motif to the CES,[41] as observed previously for similar motifs in WAPL.[43]

Cohesin-mediated LE is essential for the formation of TADs, as observed in Hi-C matrices.[12,14,16–20] A prevailing hypothesis suggests that cohesin stalls at a CTCF site on the encountering side and extrudes toward the opposite side until blocked by a second CTCF. However, single-molecule experiments revealed that cohesin rarely reverses direction after encountering CTCF,[34] and fully looped TADs are rarely observed *in vivo*.[67,68] Our findings indicate that the CTCF NTR inhibits cohesin, and the YDF motif prevents cohesin from switching direction and extruding away from the encountered CTCF.

To explore to what extent stalling of cohesin, rather than direction reversal, can explain Hi-C maps, we performed 3D polymer simulations (STAR Methods),[69,70] varying two key parameters: (1) the probability of CTCF stalling cohesin and (2) the likelihood that this stalling also prevents extrusion away from the encountered CTCF (Figure S4A). We ranked parameter combinations by the geometric standard deviation between simulated contact frequencies as a function of genomic distance *s* [P(s)] and experimental P(s) curves from Haarhuis et al.[31] and Fudenberg et al.[70] Simulations in which the majority of cohesins were prevented from switching direction upon encountering CTCF outperformed those with one-sided stalling, resembling experimental Hi-C data more closely (Figures S4B and S4C). For example, the highest-ranking simulation (where CTCF stalls cohesin with 95% probability and symmetrically blocks extrusion 75% of the time; Figure S4F) produced fewer secondary CTCF-CTCF loops than its counterpart assuming one-sided stalling (Figure S4G), aligning well with experimental Hi-C maps[31] (Figure S4H). We also explored whether cohesin can be stalled by CTCF during diffusion and slipping phases (and not only during active extrusion phases) but this had a negligible impact (Figures S4D and S4E; STAR Methods). Furthermore, we compared the colocalization of CTCF and cohesin using experimentally reported[31] and simulated chromatin immunoprecipitation sequencing (ChIP-seq) tracks (Figures S4I–S4K). *In vivo*, 41.5% of CTCF peaks were reported to colocalize with an SMC1 peak, and 95.1% of the SMC1 peaks colocalized with a CTCF peak. Analogous to the comparison of contact matrices, we ranked simulations by their agreement with these experimentally obtained values. Overall, simulations in which CTCF prevents cohesin from switching directions with a non-zero probability were in better agreement with *in vivo* colocalization data. Finally, we computed the fraction of time during which a TAD is fully looped in order to compare with recent single-particle-tracking data of fluorescently labeled, CTCF-delimited TAD boundaries.[58] The authors reported a relatively low fraction of time during which the TAD exists in a fully looped state. In our simulations, we found that TADs exist in a fully looped state 6.7% of the time when CTCF stalls cohesin

on both sides ≥90% of the time. This is in excellent agreement with previous experimental observations of ∼6% (Gabriele et al.[67]), and this fraction increases to 14.3% in our simulations when continued extrusion on the non-CTCF-bound side is allowed < 90% of the time.

These results support the notion that CTCF NTR largely inhibits cohesin upon encounter, rarely allowing extrusion away from CTCF. Instead, CTCF-CTCF loops may be formed *in vivo* by dimerization of cohesin^{STAG2} (Brunner et al.[71]). Taken together, the simulations indicate that experimentally observed Hi-C maps, ChIP-seq, and imaging data are well explained by stalled cohesin, which does not extrude away from encountered CTCF sites (Figure S4). The YDF motif biases cohesin toward unidirectional extrusion by strengthening the DNA affinity of STAG1 to DNA (Figure 2H), likely preventing DNA strand exchanges. The wild-type NTR reduces cohesin's activity most significantly, followed by NTR^{FDF} and the YDF motif alone. The effect of the YDF peptide is dependent on the YDF motif, as mutation to ADA alleviates this inhibition (Figures S2I and S2J). Whereas the YDF motif alone increases the fraction of reversals relative to consecutive steps, the full NTR reduces both (Figures 2K and 2L; Figures S3K and S3L). We conclude that CTCF's NTR regulates cohesin activity through mechanisms that extend beyond the YDF motif alone.

The KTYQR motif in the CTCF NTR inhibits cohesin-mediated LE

Nora et al.[49] identified CTCF regions that impact TAD insulation, including the NTR (NTR$^{\Delta1-89}$), an RNA-binding zinc-finger domain (NTR$^{264-288}$), and YDF motif. We evaluated NTR$^{1-89}$, which contains a conserved KTYQR motif at residues 23–27 (Figure 3A; Figure S2B) that is known to bind PDS5A.[49] We tested the effect of a fragment containing the KTYQR motif (residues 16–31; "KTYQR peptide"; Figure 3B; Table S1) on cohesin's LE dynamics and found that it strongly affected it: the KTYQR peptide reduced cohesin's ATPase activity by ∼60%, similar to the YDF peptide (Figure 3C), and it halved the frequency of active LE phases (Figure 3D), comparable to the NTR^{FDF} and NTR^{ADA} mutants, although it did not affect the LE rate (Figure S5B) or directionality (Figure 3E).

To probe the effects of the NTR without the KTYQR motif on cohesin, we expressed and purified an N-terminal truncation of the NTR (NTR$^{\Delta1-89}$) as well as an alanine-substituted mutant (NTR^{23-27A}; Figure 3B; Figure S5A; Table S1). Both variants caused only a modest reduction in LE frequency (20% and 25% lower median values, respectively; Figure 3D), suggesting that the KTYQR motif is the major determinant. Although they did not affect the LE rate (Figure S5B), both variants converted cohesin into a unidirectional extruder (Figure 3E), consistent with the major role of the YDF motif in setting the directionality.

In MT experiments, the KTYQR peptide significantly reduced cohesin's LE activity (Figures 3F and 3G; Figures S3C–S3E), achieving effects similar to 2 μM YDF peptide, but the inhibiting effect appears at lower concentrations (Figures 2I, 3F, and 3G). By contrast, the N-terminal truncation NTR$^{\Delta1-89}$ and the alanine-substituted mutant NTR^{23-27A} showed no noticeable reduction in LE activity (Figure 3G). Unlike YDF, the KTYQR peptide reduced both consecutive and reversal steps equally (Figures 3H and 3I; Figures S5H and S5I). NTR variants lacking KTYQR (NTR$^{\Delta1-89}$ and NTR^{23-27A}) did not affect overall LE activity (Figures 3F and 3G; Figures S5F and S5G) but increased the occurrence of reversals while reducing consecutive steps (Figures S5H and S5I), thereby raising the ratio of reversals to consecutive steps (Figures 3H and 3I). These findings suggest that the absence of the KTYQR motif amplifies the YDF motif's effect in the NTR, favoring reversal steps at the expense of productive extrusion.

Previously, it was shown that the CTCF NTR—in particular the YDF motif—stabilizes cohesin-mediated loops.[41] To assess whether the CTCF NTR (or any fragment thereof) increases the loop lifetime *in vitro*, we measured the lifetime of extruded loops in control experiments and in experiments including NTR peptides (Figure S5N). We found no significant changes, pointing to an effect beyond the pure interaction between cohesin and CTCF NTR, possibly via an interplay of CTCF and WAPL *in vivo*.

We thus conclude that the YDF and KTYQR motifs of the NTR of CTCF distinctly and independently affect cohesin-mediated LE action. Although both motifs suppress cohesin's overall activity (Figure 3G), they exhibit different effects on LE dynamics: the YDF motif preferentially inhibits consecutive LE steps at lower concentrations, while KTYQR reduces both consecutive and reversal steps without altering extrusion directionality.

Finally, we examined whether the combined effect of the YDF and KTYQR peptide fragments could replicate the effect of the full NTR on cohesin-mediated LE. In MT experiments, adding both peptides reduced cohesin's LE activity significantly more than either peptide alone but still less than their additive individual effects or the full NTR (Figures 3J and 3K). Notably, the combination of YDF and KTYQR peptides impaired cohesin's ability to take consecutive LE steps to a degree similar to the full NTR and surpassing the effect that the YDF peptide has alone (Figure S5L). However, their effect on reversal steps was intermediate between that of the individual peptides and the full NTR (Figure S5M), reducing the effect on the ratio of consecutive to reversal steps (Figure S5K; Figure 3L). These results suggest that the full NTR exerts additional suppression on reversal steps, while the YDF and KTYQR motifs together account for a large part of the effect NTR has on the complete inhibition of consecutive LE activity.

CTCF and cohesin are predicted to interact through KTYQR binding to STAG1 and YDF binding to STAG1 and the hinge

The YDF motif binds to cohesin at the CES, a surface formed by STAG1/2 and Scc1.[41–47] To explore whether and how other CTCF NTR regions, such as the KTYQR peptide, bind to and affect cohesin, we used AlphaFold-Multimer[72,73] to predict putative binding sites across cohesin subunits and CTCF NTR fragments. Cohesin was segmented into subunits (NIPBL-Mau2, STAG1/2, ATPase heads, and hinge regions with Scc1 segments; STAR Methods; Tables S2 and S3) and CTCF was divided into three overlapping fragments (#1: 1–100, including KTYQR; #2: 90–190; and #3 180–264, including YDF; Table S2).

AlphaFold predicted interactions between STAG1/2 and CTCF fragments #1 and #3 (Figure 4A; Figures S6A–S6C) and between the Smc hinge and fragment #3 (Figures S6D and

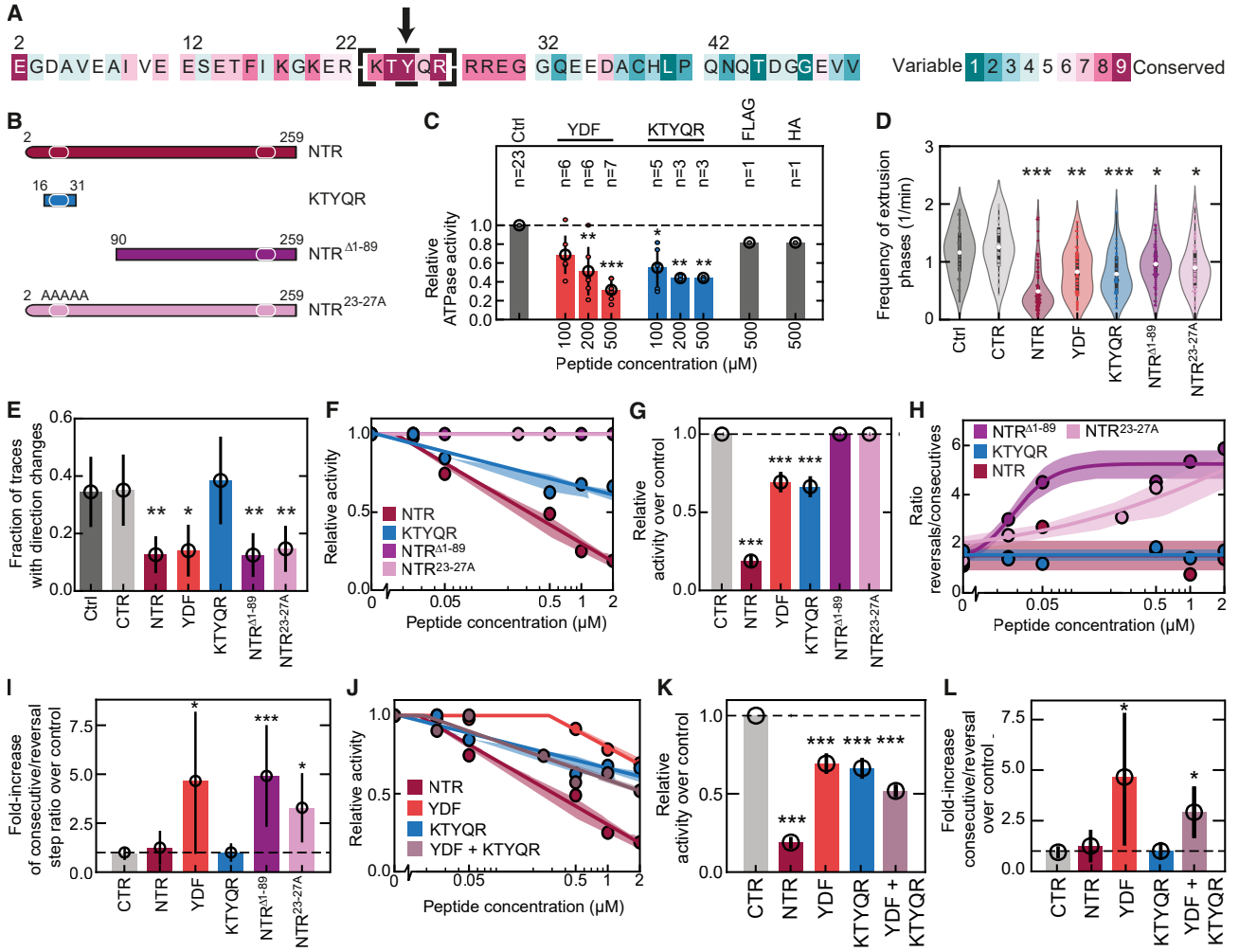

Figure 3. CTCF's KTYQR and YDF motifs inhibit LE by cohesin

(A) Conservation annotation of the human CTCF sequence surrounding the KTYQR motif.

(B) Illustration of the short KTYQR peptide as well as CTCF NTR and the corresponding truncation and mutation.

(C) Normalized ATPase activity of cohesin in the presence of the indicated concentration of CTCF peptide.

(D) Violin plot of the frequency with which extrusion phases occur in the presence of 2 μM of various CTCF fragments, as in Figures 1D and 2D. $n = 45$, 40, 91, 19, 29, 62, and 58 DNA molecules from left to right.

(E) Fraction of traces that show direction changes in the absence (control) or the presence of 2 μM of the indicated CTCF fragment. $n = 58$, 57, 103, 21, 39, 72, and 75 DNA molecules from left to right.

(F) Relative LE activity of cohesin, compared with the control ([peptide] = 0 μM), for increasing concentrations of the indicated peptides as in Figures 1I and 2I. Data correspond to the red bar height of panels Figures 1H and S5E–S5G. Fits serve as a guide for the eye (STAR Methods). Lines denote the fit and the shaded error bars denote the interpolated SD of individual data points.

(G) Relative LE activity for various peptides at 2 μM, compared with control. Error bars denote the standard deviation from repeated experiments. Statistical significance was assessed by a one-sided Welch's *t* test (**$p < 0.01$; ***$p < 0.001$).

(H) The ratio of reversals to consecutive steps at increasing concentrations of the indicated peptides, from data in Figures 1H and S5E–S5G.

(I) Ratio of reversals to consecutive steps for 2 μM of the indicated peptides, as in (G).

(J) Relative LE activity of cohesin, compared with the control ([peptide] = 0 μM), versus concentration of the indicated peptides as in Figures 1I, 2I, and 3F. The data correspond to the inverse of the red bar height of panels Figures 1H, S3F, S5E, and S5J.

(K) Ratio of reversals to consecutive steps at increasing concentrations of the indicated peptides, from data as in (J).

(L) The ratio of reversals to consecutive steps for 2 μM of the indicated peptides for the same data as in (J).

S6E). Consistent with previous experimental findings, interactions between STAG1/2 and fragment #3 were mediated by the CES and the YDF motif.[41] A new finding, however, is that in most predictions (16/25 or 25/25 for STAG1 and STAG2, respectively), the KTYQR motif was found to bind to a conserved surface, N-terminal to the CES (Figure 4A; Figures S6A and S6B). As AlphaFold does not quantitate binding affinities, the KTYQR motif may bind transiently or with low affinity, making it

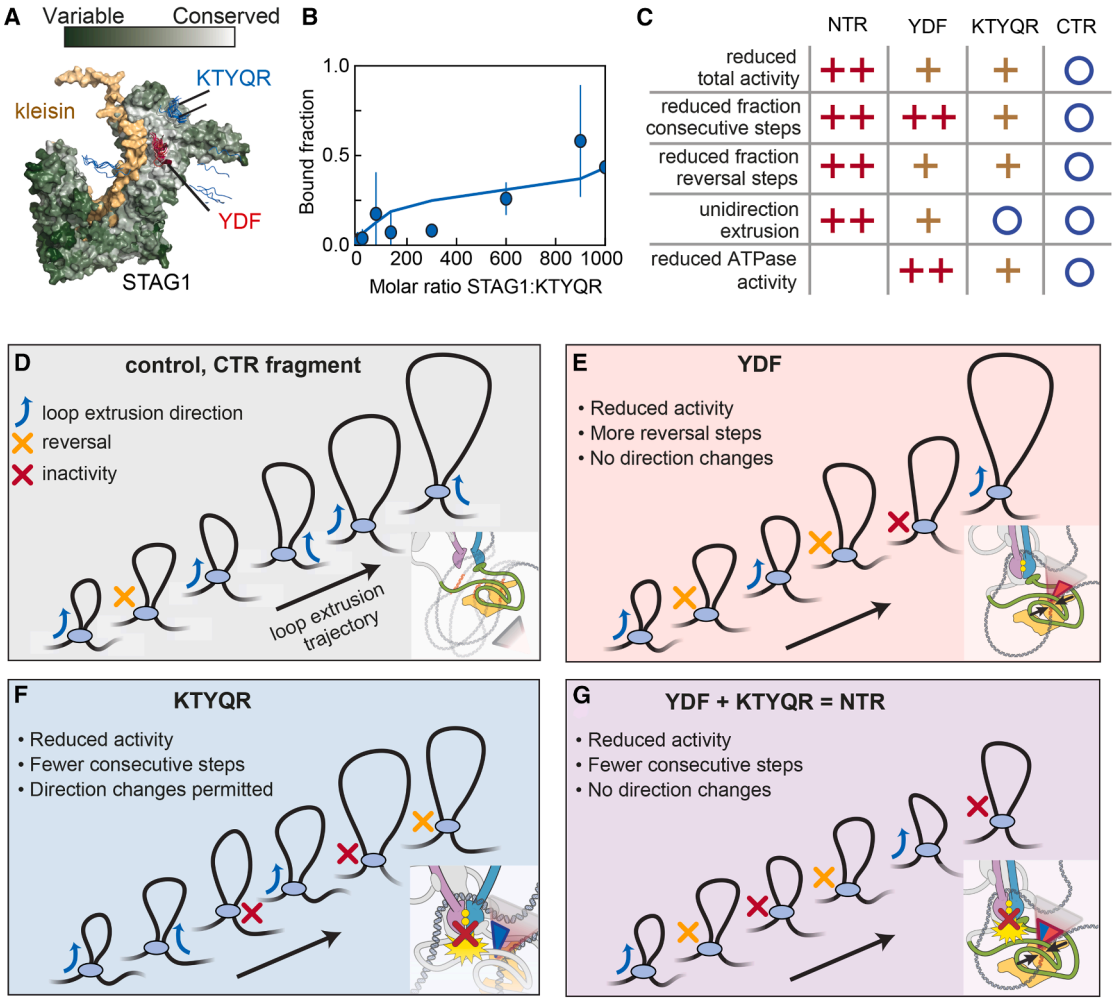

Figure 4. CTCF's YDF and KTYQR account for most of CTCF's effect on cohesin

(A) AlphaFold prediction of the STAG1^{Scc1} complex and 25 predictions of the placement of the YDF and KTYYQR peptides. STAG1 was colored according to the conservation score (STAR Methods).

(B) Fraction of fluorescently labeled KTYQR peptide bound to STAG1 versus the molar ratio of STAG1 to KTYQR peptide (STAR Methods). Experiments were conducted with two biological replicates and 4–9 technical replicates. Data points and error bars represent the mean ± SD of these replicates, while solid lines display a Savitzky-Golay-smoothed (window of 7 points, order 1) trend of the means.

(C) Overview of the effect of the NTR, YDF motif, KTYQR motif, and CTR on various characteristics of LE by cohesin (O: no effect; +: intermediate effect; ++: strong effect).

(D–G) Illustrations of the effect of the YDF, KTYQR, and their combination on DNA LE by cohesin. Without YDF or the KTYQR motif, DNA is bound relatively weakly to STAG1, potentially allowing occasional direction changes via DNA strand exchange. Binding of YDF to the STAG1 CES increases DNA affinity, preventing strand exchange and forcing unidirectional extrusion. KTYQR binds STAG1 adjacent to the CES and reduces ATP hydrolysis, lowering LE activity while still allowing direction changes. Together, these two motifs combine unidirectional LE with ATPase inhibition.

challenging to detect in bulk[41] or with *in vivo* binding assays.[49] To experimentally test the AlphaFold prediction, we performed FCS using a fluorescently labeled KTYQR peptide and purified STAG1 (STAR Methods). Increasing the molar ratio of STAG1 over the KTYQR peptide showed an increasing fraction of KTYQR peptide with a diffusion constant corresponding to a STAG1^{KTYQR} complex (STAR Methods; Figure 4B), indicating that KTYQR indeed binds to STAG1.

AlphaFold also predicted an interaction between the YDF motif and the Smc hinge in 18/25 predictions (Figures S6D and S6E). This interaction might regulate LE by cohesin and the hinge opening to modulate sister chromatid cohesion.[74–77] Supporting this, Nagasaka et al.[78] identified a separation-of-function mutant (SMC1$^{K540D/K637D/K648D}$) that retains LE but is defective in cohesion, similar to other hinge mutants previously identified in yeast.[77] Curiously, this mutant was also reduced in forming CTCF-anchored loops but not TADs *in vivo*.[78] It is tempting to speculate that an interaction between the cohesin hinge and YDF inhibits LE and thus contributes to the formation of CTCF-anchored loops. This might also modulate cohesin's tendency to undergo unsuccessful LE step cycles (reversals) due to changes in the DNA-binding affinity of the Smc hinge, which is

involved in LE.[79] However, these effects remain speculative and will need to be experimentally tested.

Together, the results suggest that the KTYQR motif inhibits cohesin by binding to STAG1/2, while the YDF motif may regulate LE through interactions with the CES and the hinge. Possibly, the YDF-hinge interaction may also regulate cohesion.

DISCUSSION

Our study provides mechanistic insights into how CTCF inhibits cohesin-mediated LE.[12,14,16–18,20,34,35,80] Our data clearly show that the NTR—rather than the CTR of CTCF—is responsible for the interaction with cohesin. Nevertheless, prior *in vitro* studies observed that cohesin was also able to halt LE when approached from the C-terminal side of CTCF.[34] Our findings suggest that in such cases, cohesin may interact with CTCF's N terminus. Supporting this, the residence times of cohesin and CTCF are similar between N- and C-terminal encounters.[34]

Although previous studies established CTCF's crucial role in stalling cohesin, implying YDF-CES binding of STAG1/2 *in vivo*,[41] the molecular details remained unclear. To reveal the underlying mechanism, we studied the effects of the CTCF NTR on cohesin-mediated LE *in vitro* and revealed the individual contributions of the YDF and KTYQR motifs therein (Figure 4C). The YDF motif reduces cohesin's activity by decreasing ATPase activity, reducing consecutive loop-extrusion steps, and driving extrusion unidirectionally by increasing STAG1's DNA-binding affinity, which presumably prevents DNA strand exchange (Figures 2, 4D, and 4F).[65,66,81] Although the KTYQR motif also reduces ATPase activity, it halts overall LE activity, in contrast to YDF (Figures 3F, 3G, and 4E). Combined, these two motifs fully suppress cohesin's ability to take consecutive LE steps (Figures 3J–3L and 4G).

Although previous studies oftentimes assumed that cohesin is converted into a unidirectional extruder upon CTCF encounter,[31,67] our results instead suggest that CTCF-bound cohesin complexes do not further extrude DNA on the unbound side. This finding could help explain the low fraction of time during which a TAD is fully looped.[67] Together, these insights help explain how CTCF establishes TAD boundaries by halting rather than redirecting cohesin-mediated LE. TADs formed by cohesin and CTCF also provide an environment that facilitates the functional establishment of enhancer-promoter contacts,[82,83] thereby contributing to the gene-regulatory network of the genome. In addition, cohesin and CTCF are directly involved in regulating specific enhancer-promoter interactions.[21,22,84,85] These regulatory sequences are often located at large genomic distances (>100 kbp).[86,87] Cohesin and CTCF therefore appear to be critical for enabling long-range enhancer-promoter interactions that would otherwise be highly improbable. Moreover, binding of CTCF between enhancers and promoters in the correct orientation provides a mechanism by which cells can control the expression of the affected genes.

Furthermore, it will be interesting to test whether transcription factors like YY1[88] or Mediator[89] can stall LE by cohesin and whether this stalling is analogous to the CTCF of potentially different cohesin-interacting motifs[90,91] that permit extrusion on the opposite side of the roadblock. Understanding how the landscape of motifs beyond CTCF (e.g., on the replisome,[27,28] the transcription machinery,[92] and examples cited above) differentially regulate cohesin activity may further elucidate the governing rules of genome architecture and function and inform therapeutic strategies for cohesinopathies and cancers where CTCF, cohesin, or other loop-extrusion-altering processes are disrupted.

Our study reveals that CTCF's NTR modulates cohesin's LE activity and directionality through its YDF and KTYQR motifs via distinct, independent mechanisms. Future studies may aim to capture the temporal sequence of conformational changes in cohesin leading to LE to further elucidate the particular binding states within the LE cycle. Such studies could also address in more detail how modulating STAG1's DNA-binding affinity leads to a change in both the cohesin's ATPase activity and the LE initiation efficiency.

Limitations of the study

We dissected the CTCF N terminus to interrogate in detail which parts cause cohesin to stall DNA LE upon encountering DNA-bound CTCF. We first characterized the previously established YDF motif and then extended this to the KTYQR motif, both of which affect cohesin's LE dynamics and efficiency. We observed that the combined YDF and KTYQR motifs do not yet fully explain the loss of activity observed with the complete CTCF NTR. Thus, our experiments do address two major factors, but not all contributions, of the NTR to cohesin. It is possible that the polymeric nature of the NTR (as the YDF and KTYQR motifs lie on the same peptide) enables the two motifs to act more cooperatively than they would as two separate short peptides in solution. Also, flanking amino acids or yet another motif might contribute to the enhanced effect of the full NTR compared with the YDF and KTYQR motifs in isolation.

Furthermore, we used AlphaFold predictions to evaluate the putative NTR-cohesin binding regions. Here, the computationally identified YDF-hinge interaction remains speculative, as further mutagenesis experiments are needed to experimentally verify its role.

Finally, although STAG1 and STAG2 form distinct complexes *in vivo*, all experiments in this manuscript were carried out using cohesin^{STAG1}. However, due to the high sequence similarity between STAG1 and STAG2 in their central regions, to which the N terminus of CTCF is thought to bind, we do not expect differences between STAG1 and STAG2.

RESOURCE AVAILABILITY

Lead contact

Requests for further information and resources should be directed to, and will be fulfilled by, the lead contact, Cees Dekker (C.Dekker@tudelft.nl).

Materials availability

All plasmids generated in this study are available from the lead contact with a completed materials transfer agreement.

Data and code availability

- Sample single-molecule fluorescence data of cohesin-mediated DNA LE (raw and median filtered data with 200 ms frame time) have been deposited on Zenodo (https://doi.org/10.5281/zenodo.16710550).[93] Access to the full dataset (that is too large for deposition on public

repository) and any additional information required to reanalyze the data reported in this study is available from the lead contact upon request.

- Original Python code to analyze MTs and AlphaFold data has been deposited on Zenodo (https://doi.org/10.5281/zenodo.15036494).[94] Original Python code to analyze single-molecule fluorescence data has been deposited on Zenodo (https://doi.org/10.5281/zenodo.10420524).[15,95]
- Any additional information required to reanalyze the data reported in this paper is available from the lead contact upon request.

ACKNOWLEDGMENTS

We thank Brian Analikwu, Allard Katan, and Miloš Tišma for discussions; Mathias Madalinski for purifying Atto550- and JF646-HaloTag ligands, as well as for synthesizing the fluorescently labeled KTYQR peptide; Melanie Panarotto for purifying STAG1; and Marcel van den Broek for help with setting up AlphaFold2. The authors acknowledge the use of computational resources of the DelftBlue supercomputer, provided by Delft High Performance Computing Centre (https://www.tudelft.nl/dhpc). J.-M.P. is also an adjunct professor at the Medical University of Vienna. Research in the laboratory of C.D. is supported by European Research Council advanced grant 883684 (DNA looping), as well as the BaSyc and the EVOLF programs. Research in the laboratory of J.-M.P. is supported by Boehringer Ingelheim, the Austrian ResearchPromotion Agency Headquarter grant (FFG-FO999902549), the European Research Council Horizon 2020 Research and Innovation Programme (101020558), and the Vienna Science and Technology Fund (LS19-029).

AUTHOR CONTRIBUTIONS

R.B., R.J., J.v.d.T., and C.D. designed experiments. L.M., R.B., and R.J. performed and analyzed magnetic tweezers experiments. R.B. and L.M. performed and analyzed single-molecule fluorescence experiments. I.F.D purified human cohesin, NIPBL-MAU2, and fluorescently labeled NIPBL-ΔN, CTCF(578–727), and CTCF(1–267)^{ADA}. R.B. performed and analyzed AlphaFold predictions and polymer simulations. G.L. performed ATPase experiments and analyzed the experimental results with R.B. J.v.d.T., E.v.d.S., and A.v.d.B. purified peptides and proteins. J.v.d.T. also synthesized DNA constructs. R.B., R.J., L.M., and C.D. wrote the manuscript with input from all authors. C.D. and J.-M.P. supervised the study.

DECLARATION OF INTERESTS

The authors declare no competing interests.

STAR★METHODS

Detailed methods are provided in the online version of this paper and include the following:

SUPPLEMENTAL INFORMATION

Supplemental information can be found online at https://doi.org/10.1016/j.molcel.2025.11.001.

Received: March 17, 2025
Revised: September 24, 2025
Accepted: November 3, 2025
Published: December 4, 2025

REFERENCES

1. Davidson, I.F., and Peters, J.M. (2021). Genome folding through loop extrusion by SMC complexes. Nat. Rev. Mol. Cell Biol. *22*, 445–464. https://doi.org/10.1038/s41580-021-00349-7.
2. Kim, E., Barth, R., and Dekker, C. (2023). Looping the Genome with SMC Complexes. Annu. Rev. Biochem. *92*, 15–41. https://doi.org/10.1146/annurev-biochem-032620-110506.
3. Davidson, I.F., Bauer, B., Goetz, D., Tang, W., Wutz, G., and Peters, J.M. (2019). DNA loop extrusion by human cohesin. Science *366*, 1338–1345. https://doi.org/10.1126/science.aaz3418.
4. Ganji, M., Shaltiel, I.A., Bisht, S., Kim, E., Kalichava, A., Haering, C.H., and Dekker, C. (2018). Real-time imaging of DNA loop extrusion by condensin. Science *360*, 102–105. https://doi.org/10.1126/science.aar7831.
5. Golfier, S., Quail, T., Kimura, H., and Brugués, J. (2020). Cohesin and condensin extrude DNA loops in a cell cycle-dependent manner. eLife *9*, e53885. https://doi.org/10.7554/eLife.53885.
6. Higashi, T.L., Pobegalov, G., Tang, M., Molodtsov, M.I., and Uhlmann, F. (2021). A brownian ratchet model for dna loop extrusion by the cohesin complex. eLife *10*, e67530. https://doi.org/10.7554/eLife.67530.
7. Kim, Y., Shi, Z., Zhang, H., Finkelstein, I.J., and Yu, H. (2019). Human cohesin compacts DNA by loop extrusion. Science *366*, 1345–1349. https://doi.org/10.1126/science.aaz4475.
8. Kong, M., Cutts, E.E., Pan, D., Beuron, F., Kaliyappan, T., Xue, C., Morris, E.P., Musacchio, A., Vannini, A., and Greene, E.C. (2020). Human Condensin I and II Drive Extensive ATP-Dependent Compaction of Nucleosome-Bound DNA. Mol. Cell *79*, 99–114.e9. https://doi.org/10.1016/j.molcel.2020.04.026.
9. Pradhan, B., Kanno, T., Umeda Igarashi, M., Loke, M.S., Baaske, M.D., Wong, J.S.K., Jeppsson, K., Björkegren, C., and Kim, E. (2023). The Smc5/6 complex is a DNA loop-extruding motor. Nature *616*, 843–848. https://doi.org/10.1038/s41586-023-05963-3.
10. Tang, M., Pobegalov, G., Tanizawa, H., Chen, Z.A., Rappsilber, J., Molodtsov, M., Noma, K.I., and Uhlmann, F. (2023). Establishment of dsDNA-dsDNA interactions by the condensin complex. Mol. Cell *83*, 3787–3800.e9. https://doi.org/10.1016/j.molcel.2023.09.019.
11. Gassler, J., Brandão, H.B., Imakaev, M., Flyamer, I.M., Ladstätter, S., Bickmore, W.A., Peters, J.M., Mirny, L.A., and Tachibana, K. (2017). A mechanism of cohesin-dependent loop extrusion organizes zygotic genome architecture. EMBO J. *36*, 3600–3618. https://doi.org/10.15252/embj.201798083.

12. Rao, S.S.P., Huang, S.C., Glenn St Hilaire, B., Engreitz, J.M., Perez, E.M., Kieffer-Kwon, K.R., Sanborn, A.L., Johnstone, S.E., Bascom, G.D., Bochkov, I.D., et al. (2017). Cohesin Loss Eliminates All Loop Domains. Cell *171*, 305–320.e24. https://doi.org/10.1016/j.cell.2017.09.026.

13. Schwarzer, W., Abdennur, N., Goloborodko, A., Pekowska, A., Fudenberg, G., Loe-Mie, Y., Fonseca, N.A., Huber, W., Haering, C.H., Mirny, L., et al. (2017). Two independent modes of chromatin organization revealed by cohesin removal. Nature *551*, 51–56. https://doi.org/10.1038/nature24281.

14. Wutz, G., Várnai, C., Nagasaka, K., Cisneros, D.A., Stocsits, R.R., Tang, W., Schoenfelder, S., Jessberger, G., Muhar, M., Hossain, M.J., et al. (2017). Topologically associating domains and chromatin loops depend on cohesin and are regulated by CTCF, WAPL, and PDS5 proteins. EMBO J. *36*, 3573–3599. https://doi.org/10.15252/embj.201798004.

15. Barth, R., Davidson, I.F., Van Der Torre, J., Taschner, M., Gruber, S., Peters, J.-M., and Dekker, C. (2025). SMC motor proteins extrude DNA asymmetrically and can switch directions. Cell *188*, 749–763.e21. https://doi.org/10.1016/j.cell.2024.12.020.

16. Nora, E.P., Goloborodko, A., Valton, A.L., Gibcus, J.H., Uebersohn, A., Abdennur, N., Dekker, J., Mirny, L.A., and Bruneau, B.G. (2017). Targeted Degradation of CTCF Decouples Local Insulation of Chromosome Domains from Genomic Compartmentalization. Cell *169*, 930–944.e22. https://doi.org/10.1016/j.cell.2017.05.004.

17. Busslinger, G.A., Stocsits, R.R., Van Der Lelij, P., Axelsson, E., Tedeschi, A., Galjart, N., and Peters, J.M. (2017). Cohesin is positioned in mammalian genomes by transcription, CTCF and Wapl. Nature *544*, 503–507. https://doi.org/10.1038/nature22063.

18. Dixon, J.R., Selvaraj, S., Yue, F., Kim, A., Li, Y., Shen, Y., Hu, M., Liu, J.S., and Ren, B. (2012). Topological domains in mammalian genomes identified by analysis of chromatin interactions. Nature *485*, 376–380. https://doi.org/10.1038/nature11082.

19. Hansen, A.S., Cattoglio, C., Darzacq, X., and Tjian, R. (2018). Recent evidence that TADs and chromatin loops are dynamic structures. Nucleus *9*, 20–32. https://doi.org/10.1080/19491034.2017.1389365.

20. Nora, E.P., Lajoie, B.R., Schulz, E.G., Giorgetti, L., Okamoto, I., Servant, N., Piolot, T., Van Berkum, N.L., Meisig, J., Sedat, J., et al. (2012). Spatial partitioning of the regulatory landscape of the X-inactivation centre. Nature *485*, 381–385. https://doi.org/10.1038/nature11049.

21. Rinzema, N.J., Sofiadis, K., Tjalsma, S.J.D., Verstegen, M.J.A.M., Oz, Y., Valdes-Quezada, C., Felder, A.-K., Filipovska, T., Van Der Elst, S., De Andrade Dos Ramos, Z., et al. (2022). Building regulatory landscapes reveals that an enhancer can recruit cohesin to create contact domains, engage CTCF sites and activate distant genes. Nat. Struct. Mol. Biol. *29*, 563–574. https://doi.org/10.1038/s41594-022-00787-7.

22. Kane, L., Williamson, I., Flyamer, I.M., Kumar, Y., Hill, R.E., Lettice, L.A., and Bickmore, W.A. (2022). Cohesin is required for long-range enhancer action at the Shh locus. Nat. Struct. Mol. Biol. *29*, 891–897. https://doi.org/10.1038/s41594-022-00821-8.

23. Kiefer, L., Chiosso, A., Langen, J., Buckley, A., Gaudin, S., Rajkumar, S.M., Servito, G.I.F., Cha, E.S., Vijay, A., Yeung, A., et al. (2023). WAPL functions as a rheostat of Protocadherin isoform diversity that controls neural wiring. Science *380*, eadf8440. https://doi.org/10.1126/science.adf8440.

24. Ball, A.R., Chen, Y.-Y., and Yokomori, K. (2014). Mechanisms of cohesin-mediated gene regulation and lessons learned from cohesinopathies. Biochim. Biophys. Acta *1839*, 191–202. https://doi.org/10.1016/j.bbagrm.2013.11.002.

25. Horsfield, J.A. (2022). Full circle: a brief history of cohesin and the regulation of gene expression. FEBS J. *290*, 1670–1687. https://doi.org/10.1111/febs.16362.

26. Emerson, D.J., Zhao, P.A., Cook, A.L., Barnett, R.J., Klein, K.N., Saulebekova, D., Ge, C., Zhou, L., Simandi, Z., Minsk, M.K., et al. (2022). Cohesin-mediated loop anchors confine the locations of human replication origins. Nature *606*, 812–819. https://doi.org/10.1038/s41586-022-04803-0.

27. Liao, Q., Brandão, H.B., Ren, Z., and Wang, X. (2025). Replisomes restrict SMC translocation in vivo. Nat. Commun. *16*, 7151. https://doi.org/10.1038/s41467-025-62596-y.

28. Dequeker, B.J.H., Scherr, M.J., Brandão, H.B., Gassler, J., Powell, S., Gaspar, I., Flyamer, I.M., Lalic, A., Tang, W., Stocsits, R., et al. (2022). MCM complexes are barriers that restrict cohesin-mediated loop extrusion. Nature *606*, 197–203. https://doi.org/10.1038/s41586-022-04730-0.

29. Rao, S.S.P., Huntley, M.H., Durand, N.C., Stamenova, E.K., Bochkov, I.D., Robinson, J.T., Sanborn, A.L., Machol, I., Omer, A.D., Lander, E.S., et al. (2014). A 3D map of the human genome at kilobase resolution reveals principles of chromatin looping. Cell *159*, 1665–1680. https://doi.org/10.1016/j.cell.2014.11.021.

30. Guo, Y., Xu, Q., Canzio, D., Shou, J., Li, J., Gorkin, D.U., Jung, I., Wu, H., Zhai, Y., Tang, Y., et al. (2015). CRISPR Inversion of CTCF Sites Alters Genome Topology and Enhancer/Promoter Function. Cell *162*, 900–910. https://doi.org/10.1016/j.cell.2015.07.038.

31. Haarhuis, J.H.I., van der Weide, R.H., Blomen, V.A., Yáñez-Cuna, J.O., Amendola, M., van Ruiten, M.S., Krijger, P.H.L., Teunissen, H., Medema, R.H., van Steensel, B., et al. (2017). The Cohesin Release Factor WAPL Restricts Chromatin Loop Extension. Cell *169*, 693–707.e14. https://doi.org/10.1016/j.cell.2017.04.013.

32. Tang, Z., Luo, O.J., Li, X., Zheng, M., Zhu, J.J., Szalaj, P., Trzaskoma, P., Magalska, A., Wlodarczyk, J., Ruszczycki, B., et al. (2015). CTCF-Mediated Human 3D Genome Architecture Reveals Chromatin Topology for Transcription. Cell *163*, 1611–1627. https://doi.org/10.1016/j.cell.2015.11.024.

33. de Wit, E., Vos, E.S.M., Holwerda, S.J.B., Valdes-Quezada, C., Verstegen, M.J.A.M., Teunissen, H., Splinter, E., Wijchers, P.J., Krijger, P.H.L., and de Laat, W. (2015). CTCF Binding Polarity Determines Chromatin Looping. Mol. Cell *60*, 676–684. https://doi.org/10.1016/j.molcel.2015.09.023.

34. Davidson, I.F., Barth, R., Zaczek, M., Van Der Torre, J., Tang, W., Nagasaka, K., Janissen, R., Kerssemakers, J., Wutz, G., Dekker, C., et al. (2023). CTCF is a DNA-tension-dependent barrier to cohesin-mediated loop extrusion. Nature *616*, 822–827. https://doi.org/10.1038/s41586-023-05961-5.

35. Zhang, H., Shi, Z., Banigan, E.J., Kim, Y., Yu, H., Bai, X.C., and Finkelstein, I.J. (2023). CTCF and R-loops are boundaries of cohesin-mediated DNA looping. Mol. Cell *83*, 2856–2871.e8. https://doi.org/10.1016/j.molcel.2023.07.006.

36. Hansen, A.S., Pustova, I., Cattoglio, C., Tjian, R., and Darzacq, X. (2017). CTCF and cohesin regulate chromatin loop stability with distinct dynamics. eLife *6*, e25776. https://doi.org/10.7554/elife.25776.

37. Hansen, A.S., Hsieh, T.S., Cattoglio, C., Pustova, I., Saldaña-Meyer, R., Reinberg, D., Darzacq, X., and Tjian, R. (2019). Distinct Classes of Chromatin Loops Revealed by Deletion of an RNA-Binding Region in CTCF. Mol. Cell *76*, 395–411.e13. https://doi.org/10.1016/j.molcel.2019.07.039.

38. Parelho, V., Hadjur, S., Spivakov, M., Leleu, M., Sauer, S., Gregson, H.C., Jarmuz, A., Canzonetta, C., Webster, Z., Nesterova, T., et al. (2008). Cohesins Functionally Associate with CTCF on Mammalian Chromosome Arms. Cell *132*, 422–433. https://doi.org/10.1016/j.cell.2008.01.011.

39. Pugacheva, E.M., Kubo, N., Loukinov, D., Tajmul, M., Kang, S., Kovalchuk, A.L., Strunnikov, A.V., Zentner, G.E., Ren, B., and Lobanenkov, V.V. (2020). CTCF mediates chromatin looping via N-terminal domain-dependent cohesin retention. Proc. Natl. Acad. Sci. USA *117*, 2020–2031. https://doi.org/10.1073/pnas.1911708117.

40. Wendt, K.S., Yoshida, K., Itoh, T., Bando, M., Koch, B., Schirghuber, E., Tsutsumi, S., Nagae, G., Ishihara, K., Mishiro, T., et al. (2008). Cohesin

mediates transcriptional insulation by CCCTC-binding factor. Nature *451*, 796–801. https://doi.org/10.1038/nature06634.

41. Li, Y., Haarhuis, J.H.I., Sedeño Cacciatore, Á., Oldenkamp, R., van Ruiten, M.S., Willems, L., Teunissen, H., Muir, K.W., de Wit, E., Rowland, B.D., et al. (2020). The structural basis for cohesin–CTCF-anchored loops. Nature *578*, 472–476. https://doi.org/10.1038/s41586-019-1910-z.
42. García-Nieto, A., Patel, A., Li, Y., Oldenkamp, R., Feletto, L., Graham, J.J., Willems, L., Muir, K.W., Panne, D., and Rowland, B.D. (2023). Structural basis of centromeric cohesion protection. Nat. Struct. Mol. Biol. *30*, 853–859. https://doi.org/10.1038/s41594-023-00968-y.
43. Hara, K., Zheng, G., Qu, Q., Liu, H., Ouyang, Z., Chen, Z., Tomchick, D.R., and Yu, H. (2014). Structure of cohesin subcomplex pinpoints direct shugoshin-Wapl antagonism in centromeric cohesion. Nat. Struct. Mol. Biol. *21*, 864–870. https://doi.org/10.1038/nsmb.2880.
44. Orgil, O., Matityahu, A., Eng, T., Guacci, V., Koshland, D., and Onn, I. (2015). A Conserved Domain in the Scc3 Subunit of Cohesin Mediates the Interaction with Both Mcd1 and the Cohesin Loader Complex. PLoS Genet. *11*, e1005036. https://doi.org/10.1371/journal.pgen.1005036.
45. Pezzi, N., Prieto, I., Kremer, L., Pérez Jurado, L.A., Valero, C., Del Mazo, J., Martínez-A, C., and Barbero, J.L. (2000). *STAG3*, a novel gene encoding a protein involved in meiotic chromosome pairing and location of *STAG3*-related genes flanking the Williams-Beuren syndrome deletion. FASEB J. *14*, 581–592. https://doi.org/10.1096/fasebj.14.3.581.
46. Roig, M.B., Löwe, J., Chan, K.-L., Beckouët, F., Metson, J., and Nasmyth, K. (2014). Structure and function of cohesin's Scc3/SA regulatory subunit. FEBS Lett. *588*, 3692–3702. https://doi.org/10.1016/j.febslet.2014.08.015.
47. Rubio, E.D., Reiss, D.J., Welcsh, P.L., Disteche, C.M., Filippova, G.N., Baliga, N.S., Aebersold, R., Ranish, J.A., and Krumm, A. (2008). CTCF physically links cohesin to chromatin. Proc. Natl. Acad. Sci. USA *105*, 8309–8314. https://doi.org/10.1073/pnas.0801273105.
48. Hansen, A.S. (2020). CTCF as a boundary factor for cohesin-mediated loop extrusion: evidence for a multi-step mechanism. Nucleus *11*, 132–148. https://doi.org/10.1080/19491034.2020.1782024.
49. Nora, E.P., Caccianini, L., Fudenberg, G., So, K., Kameswaran, V., Nagle, A., Uebersohn, A., Hajj, B., Saux, A.L., Coulon, A., et al. (2020). Molecular basis of CTCF binding polarity in genome folding. Nat. Commun. *11*, 5612. https://doi.org/10.1038/s41467-020-19283-x.
50. Saldaña-Meyer, R., Rodriguez-Hernaez, J., Escobar, T., Nishana, M., Jácome-López, K., Nora, E.P., Bruneau, B.G., Tsirigos, A., Furlan-Magaril, M., Skok, J., et al. (2019). RNA Interactions Are Essential for CTCF-Mediated Genome Organization. Mol. Cell *76*, 412–422.e5. https://doi.org/10.1016/j.molcel.2019.08.015.
51. Weiss, F.D., Calderon, L., Wang, Y.-F., Georgieva, R., Guo, Y., Cvetesic, N., Kaur, M., Dharmalingam, G., Krantz, I.D., Lenhard, B., et al. (2021). Neuronal genes deregulated in Cornelia de Lange Syndrome respond to removal and re-expression of cohesin. Nat. Commun. *12*, 2919. https://doi.org/10.1038/s41467-021-23141-9.
52. Mfarej, M.G., and Skibbens, R.V. (2020). An ever-changing landscape in Roberts syndrome biology: Implications for macromolecular damage. PLoS Genet. *16*, e1009219. https://doi.org/10.1371/journal.pgen.1009219.
53. Song, S.-H., and Kim, T.-Y. (2017). CTCF, Cohesin, and Chromatin in Human Cancer. Genomics Inform. *15*, 114–122. https://doi.org/10.5808/GI.2017.15.4.114.
54. Zhang, H., Emerson, D.J., Gilgenast, T.G., Titus, K.R., Lan, Y., Huang, P., Zhang, D., Wang, H., Keller, C.A., Giardine, B., et al. (2019). Chromatin structure dynamics during the mitosis-to-G1 phase transition. Nature *576*, 158–162. https://doi.org/10.1038/s41586-019-1778-y.
55. Hill, L., Ebert, A., Jaritz, M., Wutz, G., Nagasaka, K., Tagoh, H., Kostanova-Poliakova, D., Schindler, K., Sun, Q., Bönelt, P., et al. (2020). Wapl repression by Pax5 promotes V gene recombination by Igh loop extrusion. Nature *584*, 142–147. https://doi.org/10.1038/s41586-020-2454-y.
56. Ryu, J.-K., Rah, S.-H., Janissen, R., Kerssemakers, J.W.J., Bonato, A., Michieletto, D., and Dekker, C. (2022). Condensin extrudes DNA loops in steps up to hundreds of base pairs that are generated by ATP binding events. Nucleic Acids Res. *50*, 820–832. https://doi.org/10.1093/nar/gkab1268.
57. Davidson, I.F., Barth, R., Horn, S., Janissen, R., Nagasaka, K., Wutz, G., Stocsits, R.R., Bauer, B., Dekker, C., and Peters, J.-M. (2024). Cohesin supercoils DNA during loop extrusion. Cell Rep. *44*, 115856. https://doi.org/10.1016/j.celrep.2025.115856.
58. Janissen, R., Barth, R., Davidson, I.F., Peters, J.-M., and Dekker, C. (2024). All eukaryotic SMC proteins induce a twist of −0.6 at each DNA loop extrusion step. Sci. Adv. *10*, eadt1832. https://doi.org/10.1126/sciadv.adt1832.
59. Dekker, C., Haering, C.H., Peters, J.-M., and Rowland, B.D. (2023). How do molecular motors fold the genome? Science *382*, 646–648. https://doi.org/10.1126/science.adi8308.
60. Marko, J.F., De Los Rios, P., Barducci, A., and Gruber, S. (2019). DNA-segment-capture model for loop extrusion by structural maintenance of chromosome (SMC) protein complexes. Nucleic Acids Res. *47*, 6956–6972. https://doi.org/10.1093/nar/gkz497.
61. Nomidis, S.K., Carlon, E., Gruber, S., and Marko, J.F. (2022). DNA tension-modulated translocation and loop extrusion by SMC complexes revealed by molecular dynamics simulations. Nucleic Acids Res. *50*, 4974–4987. https://doi.org/10.1093/nar/gkac268.
62. Yamauchi, M., Brandani, G.B., Terakawa, T., and Takada, S. (2024). SMC complex unidirectionally translocates DNA by coupling segment capture with an asymmetric kleisin path. eLife *14*, RP106752. https://doi.org/10.1101/2024.04.29.591782.
63. Loeff, L., Kerssemakers, J.W.J., Joo, C., and Dekker, C. (2021). AutoStepfinder: A fast and automated step detection method for single-molecule analysis. Patterns (N Y) *2*, 100256. https://doi.org/10.1016/j.patter.2021.100256.
64. Li, J., Huang, K., Hu, G., Babarinde, I.A., Li, Y., Dong, X., Chen, Y.-S., Shang, L., Guo, W., Wang, J., et al. (2019). An alternative CTCF isoform antagonizes canonical CTCF occupancy and changes chromatin architecture to promote apoptosis. Nat. Commun. *10*, 1535. https://doi.org/10.1038/s41467-019-08949-w.
65. Barth, R., Davidson, I.F., Van Der Torre, J., Taschner, M., Gruber, S., Peters, J.-M., and Dekker, C. (2023). SMC motor proteins extrude DNA asymmetrically and contain a direction switch. Cell *188*, 749–763.e21. https://doi.org/10.1101/2023.12.21.572892.
66. Shaltiel, I.A., Datta, S., Lecomte, L., Hassler, M., Kschonsak, M., Bravo, S., Stober, C., Ormanns, J., Eustermann, S., and Haering, C.H. (2022). A hold-and-feed mechanism drives directional DNA loop extrusion by condensin. Science *376*, 1087–1094. https://doi.org/10.1126/science.abm4012.
67. Gabriele, M., Brandão, H.B., Grosse-Holz, S., Jha, A., Dailey, G.M., Cattoglio, C., Hsieh, T.H.S., Mirny, L., Zechner, C., and Hansen, A.S. (2022). Dynamics of CTCF- and cohesin-mediated chromatin looping revealed by live-cell imaging. Science *376*, 476–501. https://doi.org/10.1126/science.abn6583.
68. Mach, P., Kos, P.I., Zhan, Y., Cramard, J., Gaudin, S., Tünnermann, J., Marchi, E., Eglinger, J., Zuin, J., Kryzhanovska, M., et al. (2022). Cohesin and CTCF control the dynamics of chromosome folding. Nat. Genet. *54*, 1907–1918. https://doi.org/10.1038/s41588-022-01232-7.
69. Banigan, E.J., van den Berg, A.A., Brandão, H.B., Marko, J.F., and Mirny, L.A. (2020). Chromosome organization by one-sided and two-sided loop extrusion. eLife *9*, e53558. https://doi.org/10.7554/eLife.53558.
70. Fudenberg, G., Imakaev, M., Lu, C., Goloborodko, A., Abdennur, N., and Mirny, L.A. (2016). Formation of Chromosomal Domains by Loop

Extrusion. Cell Rep. *15*, 2038–2049. https://doi.org/10.1016/j.celrep.2016.04.085.

71. Brunner, A., Morero, N.R., Zhang, W., Hossain, M.J., Lampe, M., Pflaumer, H., Halavatyi, A., Peters, J.-M., Beckwith, K.S., and Ellenberg, J. (2025). Quantitative imaging of loop extruders rebuilding interphase genome architecture after mitosis. J. Cell Biol. *224*, e202405169. https://doi.org/10.1083/jcb.202405169.

72. Evans, R., O'Neill, M., Pritzel, A., Antropova, N., Senior, A., Green, T., Žídek, A., Bates, R., Blackwell, S., Yim, J., et al. (2021). Protein complex prediction with AlphaFold-Multimer. Preprint at bioRxiv. https://doi.org/10.1101/2021.10.04.463034.

73. Jumper, J., Evans, R., Pritzel, A., Green, T., Figurnov, M., Ronneberger, O., Tunyasuvunakool, K., Bates, R., Žídek, A., Potapenko, A., et al. (2021). Highly accurate protein structure prediction with AlphaFold. Nature *596*, 583–589. https://doi.org/10.1038/s41586-021-03819-2.

74. Collier, J.E., and Nasmyth, K.A. (2022). DNA passes through cohesin's hinge as well as its Smc3–kleisin interface. eLife *11*, e80310. https://doi.org/10.7554/eLife.80310.

75. Gruber, S., Arumugam, P., Katou, Y., Kuglitsch, D., Helmhart, W., Shirahige, K., and Nasmyth, K. (2006). Evidence that Loading of Cohesin Onto Chromosomes Involves Opening of Its SMC Hinge. Cell *127*, 523–537. https://doi.org/10.1016/j.cell.2006.08.048.

76. Robison, B., Guacci, V., and Koshland, D. (2018). A role for the Smc3 hinge domain in the maintenance of sister chromatid cohesion. Mol. Biol. Cell *29*, 339–355. https://doi.org/10.1091/mbc.E17-08-0511.

77. Srinivasan, M., Scheinost, J.C., Petela, N.J., Gligoris, T.G., Wissler, M., Ogushi, S., Collier, J.E., Voulgaris, M., Kurze, A., Chan, K.L., et al. (2018). The Cohesin Ring Uses Its Hinge to Organize DNA Using Non-topological as well as Topological Mechanisms. Cell *173*, 1508–1519.e18. https://doi.org/10.1016/j.cell.2018.04.015.

78. Nagasaka, K., Davidson, I.F., Stocsits, R.R., Tang, W., Wutz, G., Batty, P., Panarotto, M., Litos, G., Schleiffer, A., Gerlich, D.W., et al. (2023). Cohesin mediates DNA loop extrusion and sister chromatid cohesion by distinct mechanisms. Mol. Cell *83*, 3049–3063.e6. https://doi.org/10.1016/j.molcel.2023.07.024.

79. Bauer, B.W., Davidson, I.F., Canena, D., Wutz, G., Tang, W., Litos, G., Horn, S., Hinterdorfer, P., and Peters, J.M. (2021). Cohesin mediates DNA loop extrusion by a "swing and clamp" mechanism. Cell *184*, 5448–5464.e22. https://doi.org/10.1016/j.cell.2021.09.016.

80. Vietri Rudan, M., Barrington, C., Henderson, S., Ernst, C., Odom, D.T., Tanay, A., and Hadjur, S. (2015). Comparative Hi-C Reveals that CTCF Underlies Evolution of Chromosomal Domain Architecture. Cell Rep. *10*, 1297–1309. https://doi.org/10.1016/j.celrep.2015.02.004.

81. Higashi, T.L., Eickhoff, P., Sousa, J.S., Locke, J., Nans, A., Flynn, H.R., Snijders, A.P., Papageorgiou, G., O'Reilly, N., Chen, Z.A., et al. (2020). A Structure-Based Mechanism for DNA Entry into the Cohesin Ring. Mol. Cell *79*, 917–933.e9. https://doi.org/10.1016/j.molcel.2020.07.013.

82. Hsieh, T.S., Cattoglio, C., Slobodyanyuk, E., Hansen, A.S., Darzacq, X., and Tjian, R. (2022). Enhancer–promoter interactions and transcription are largely maintained upon acute loss of CTCF, cohesin, WAPL or YY1. Nat. Genet. *54*, 1919–1932. https://doi.org/10.1038/s41588-022-01223-8.

83. Karpinska, M.A., Zhu, Y., Fakhraei Ghazvini, Z., Ramasamy, S., Barbieri, M., Cao, T.B.N., Varahram, N., Aljahani, A., Lidschreiber, M., Papantonis, A., et al. (2025). CTCF depletion decouples enhancer-mediated gene activation from chromatin hub formation. Nat. Struct. Mol. Biol. *32*, 1268–1281. https://doi.org/10.1038/s41594-025-01555-z.

84. Calderon, L., Weiss, F.D., Beagan, J.A., Oliveira, M.S., Georgieva, R., Wang, Y.-F., Carroll, T.S., Dharmalingam, G., Gong, W., Tossell, K., et al. (2022). Cohesin-dependence of neuronal gene expression relates to chromatin loop length. eLife *11*, e76539. https://doi.org/10.7554/eLife.76539.

85. Aljahani, A., Hua, P., Karpinska, M.A., Quililan, K., Davies, J.O.J., and Oudelaar, A.M. (2022). Analysis of sub-kilobase chromatin topology reveals nano-scale regulatory interactions with variable dependence on cohesin and CTCF. Nat. Commun. *13*, 2139. https://doi.org/10.1038/s41467-022-29696-5.

86. Kubo, N., Ishii, H., Xiong, X., Bianco, S., Meitinger, F., Hu, R., Hocker, J.D., Conte, M., Gorkin, D., Yu, M., et al. (2021). Promoter-proximal CTCF binding promotes distal enhancer-dependent gene activation. Nat. Struct. Mol. Biol. *28*, 152–161. https://doi.org/10.1038/s41594-020-00539-5.

87. Bower, G., and Kvon, E.Z. (2025). Genetic factors mediating long-range enhancer–promoter communication in mammalian development. Curr. Opin. Genet. Dev. *90*, 102282. https://doi.org/10.1016/j.gde.2024.102282.

88. Weintraub, A.S., Li, C.H., Zamudio, A.V., Sigova, A.A., Hannett, N.M., Day, D.S., Abraham, B.J., Cohen, M.A., Nabet, B., Buckley, D.L., et al. (2017). YY1 Is a Structural Regulator of Enhancer-Promoter Loops. Cell *171*, 1573–1588.e28. https://doi.org/10.1016/j.cell.2017.11.008.

89. Kagey, M.H., Newman, J.J., Bilodeau, S., Zhan, Y., Orlando, D.A., Van Berkum, N.L., Ebmeier, C.C., Goossens, J., Rahl, P.B., Levine, S.S., et al. (2010). Mediator and cohesin connect gene expression and chromatin architecture. Nature *467*, 430–435. https://doi.org/10.1038/nature09380.

90. Lu, Z., Wang, Y., Assumpção, A.L.F.V., Liu, P., Kopp, A., Saka, S., Mcilwain, S.J., Viny, A.D., Brand, M., and Pan, X. (2024). Yin Yang 1 regulates cohesin complex protein SMC3 in mouse hematopoietic stem cells. Blood Adv. *8*, 3076–3091. https://doi.org/10.1182/bloodadvances.2023011411.

91. Pan, X., Papasani, M., Hao, Y., Calamito, M., Wei, F., Quinn, W.J., Basu, A., Wang, J., Hodawadekar, S., Zaprazna, K., et al. (2013). YY1 controls Igκ repertoire and B-cell development, and localizes with condensin on the Igκ locus. EMBO J. *32*, 1168–1182. https://doi.org/10.1038/emboj.2013.66.

92. Banigan, E.J., Tang, W., Van Den Berg, A.A., Stocsits, R.R., Wutz, G., Brandão, H.B., Busslinger, G.A., Peters, J.-M., and Mirny, L.A. (2023). Transcription shapes 3D chromatin organization by interacting with loop extrusion. Proc. Natl. Acad. Sci. USA *120*, e2210480120. https://doi.org/10.1073/pnas.2210480120.

93. Muras, L., and Barth, R. (2025). Sample data connected to Barth, Janissen, Muras et al "Two CTCF motifs impede cohesin-mediated DNA loop extrusion". Zenodo. https://doi.org/10.5281/ZENODO.16710549.

94. Barth, R., Muras, L., and Janissen, R. (2025). Python scripts used to conduct Magnetic Tweezers and AlphaFold analyses as presented in Barth, Janissen, Muras et al "Two CTCF motifs impede cohesin-mediated DNA loop extrusion". Zenodo.https://doi.org/10.5281/ZENODO.15036494.

95. Barth, R. (2024). Python scripts used to conduct analyses and simulations as presented in Barth et al "SMC motor proteins extrude DNA asymmetrically and contain a direction switch". Version 1.0. Zenodo. https://doi.org/10.5281/ZENODO.10420524.

96. Weissmann, F., and Peters, J.-M. (2018). Expressing Multi-subunit Complexes Using biGBac. In Protein Complex Assembly Methods in Molecular Biology, J.A. Marsh, ed. (Springer), pp. 329–343. https://doi.org/10.1007/978-1-4939-7759-8_21.

97. Eastman, P., and Pande, V.S. (2010). Efficient nonbonded interactions for molecular dynamics on a graphics processing unit. J. Comput. Chem. *31*, 1268–1272. https://doi.org/10.1002/jcc.21413.

98. Eastman, P., Swails, J., Chodera, J.D., McGibbon, R.T., Zhao, Y., Beauchamp, K.A., Wang, L.-P., Simmonett, A.C., Harrigan, M.P., Stern, C.D., et al. (2017). OpenMM 7: Rapid development of high performance algorithms for molecular dynamics. PLoS Comput. Biol. *13*, e1005659. https://doi.org/10.1371/journal.pcbi.1005659.

99. Goloborodko, A., Imakaev, M.V., Marko, J.F., and Mirny, L. (2016). Compaction and segregation of sister chromatids via active loop extrusion. eLife *5*, e14864. https://doi.org/10.7554/eLife.14864.

100. (DHPC), D.H.P.C.C.. (2024). DelftBlue Supercomputer (Phase 2). https://www.tudelft.nl/dhpc/ark/delftbluephase2.

101. Truong, C., Oudre, L., and Vayatis, N. (2020). Selective review of offline change point detection methods. Signal Process. *167*, 107299. https://doi.org/10.1016/j.sigpro.2019.107299.

102. Virtanen, P., Gommers, R., Oliphant, T.E., Haberland, M., Reddy, T., Cournapeau, D., Burovski, E., Peterson, P., Weckesser, W., Bright, J., et al. (2020). SciPy 1.0: fundamental algorithms for scientific computing in Python. Nat. Methods *17*, 261–272. https://doi.org/10.1038/s41592-019-0686-2.

103. Liu, H., and Shima, T. (2021). A fast and objective hidden Markov modeling for accurate analysis of biophysical data with numerous states. Preprint at bioRxiv. https://doi.org/10.1101/2021.05.30.446337.

104. Smith, D.A. (1998). A Quantitative Method for the Detection of Edges in Noisy Time-Series. Philos. Trans. R. Soc. Lond. B Biol. Sci. *353*, 1969–1981. https://doi.org/10.1098/rstb.1998.0348.

115. Jachowski, T. (2023). tobiasjj/stepfinder. GitHub. https://github.com/tobiasjj/stepfinder.

106. Chung, S.H., and Kennedy, R.A. (1991). Forward-backward non-linear filtering technique for extracting small biological signals from noise. J. Neurosci. Methods *40*, 71–86. https://doi.org/10.1016/0165-0270(91)90118-J.

107. Schrimpf, W., Barth, A., Hendrix, J., and Lamb, D.C. (2018). PAM: A Framework for Integrated Analysis of Imaging, Single-Molecule, and Ensemble Fluorescence Data. Biophys. J. *114*, 1518–1528. https://doi.org/10.1016/j.bpj.2018.02.035.

108. Kapusta, P. (2010). Absolute diffusion coefficients: compilation of reference data for FCS calibration. https://www.picoquant.com/images/uploads/page/files/7353/appnote_diffusioncoefficients.pdf.

109. Berezin, C., Glaser, F., Rosenberg, J., Paz, I., Pupko, T., Fariselli, P., Casadio, R., and Ben-Tal, N. (2004). ConSeq: the identification of functionally and structurally important residues in protein sequences. Bioinformatics *20*, 1322–1324. https://doi.org/10.1093/bioinformatics/bth070.

110. Yariv, B., Yariv, E., Kessel, A., Masrati, G., Chorin, A.B., Martz, E., Mayrose, I., Pupko, T., and Ben-Tal, N. (2023). Using evolutionary data to make sense of macromolecules with a "face-lifted" ConSurf. Protein Sci. *32*, e4582. https://doi.org/10.1002/pro.4582.

111. Schrödinger, LLC. (2015). The PyMOL molecular graphics system, version 1.8. https://www.pymol.org/.

STAR★METHODS

KEY RESOURCES TABLE

REAGENT or RESOURCE	SOURCE	IDENTIFIER
Antibodies		
Digoxigenin antibodies	Roche	RRID:AB_514496
Bacterial and virus strains		
E. coli DH5alpha	In-house	N/A
DH10MultiBAC DH10EmBacY	In-house	N/A
DH5-alpha	NEB	Cat#C2987
ER2566	NEB	Cat#C2566
Other		
Streptavidin-coated Superparamagnetic beads MyOne	Thermo Fischer	Cat#65601
Polystyrene beads 1.5 μm	Polysciences Europe	Cat#17133
Chemicals, peptides, and recombinant proteins		
Gamma-32-ATP	Hartmann Analytic	Cat#SCP-501
ATP	Jena Biosciences	Cat#NU-1049
Fugene 6	Promega	Cat#E2691
Ni-NTA agarose	Qiagen	Cat#30230
Flag M2 agarose beads	Sigma	Cat#A2220-25ML
Toyopearl AF-Chelate-650M	Tosoh	Cat#0014475
Pluronic F-127	Sigma	Cat#P2443
Fetal calf serum	Gibco	Cat#A5256801
L-glutamine	Gibco	Cat#25030-024
Penicillin/Streptomycin	Sigma	Cat#P0781
Poloxamer 188	Gibco	Cat#24040-032
cOmplete EDTA-free protease inhibitor	Roche	Cat#11873580001
Halo Ligand Amine O2	Promega	Cat#P6711
JF646 SE	Tocris	Cat#6148
ATTO 550 NHS-ester	ATTO-TEC	Cat#AD 550-35
nCTCF peptides	This paper; Table S1	N/A
Experimental models: Cell lines		
SF9 insect cells	Thermo Fisher Scientific	Cat#B82501
Oligonucleotides		
Lambda DNA	New England Biolabs	Cat#N3011S
Recombinant DNA		
1.5 kbp linear dsDNA for magnetic tweezers	Ryu et al.[56]	N/A
Cohesin expression plasmid (pBig2ab SMC1, SMC3-FLAG, SCC1(TEV)-HALO, HIS-STAG1; c136)	Davidson et al.[3]	N/A
NIPBL-MAU2 expression plasmid (pLib FLAG-HALO-NIPBL-HIS, MAU2; LC50A)	Davidson et al.[3]	N/A
NIPBL-DN expression plasmid (pLib FLAG-HALO-NIPBL(Δ22-1040)-HIS; BB17/241)	Bauer et al.[79]	N/A
STAG1 expression plasmid (pLib HIS-STAG1; c179)	Davidson et al.[3]	N/A
CTCF CTR expression plasmid (pLib 10xHis-CTCF(578-727)-Halo-Flag; mz92.1)	This paper	ID727

(*Continued on next page*)

Continued

REAGENT or RESOURCE	SOURCE	IDENTIFIER
CTCF NTR^{ADA} expression plasmid (pLib 10xHis-Halo-CTCF(1-267)$^{Y226A;\ F228A}$; c339)	This paper	ID267
pMal-C5X-MPB-3c-nCTCF	This paper	JT188
pMal-C5X-MPB-3c-nCTCF –FdF	This paper	JT195
pMal-C5X-MPB-3c-nCTCF -d1-89	This paper	JT191
pMal-C5X-MBP-3c-nCTCF-23-27A	This paper	2327
P-GGGCGGCGACCT-Bio	IDT	JT41
P-AGGTCGCCGCCC-Bio	IDT	JT42
Software and algorithms		
Prism V9	GraphPad	RRID:SCR_002798
LabView 2011	National Instruments	RRID:SCR_014325
IgorPro V6.37	Wavemetrics	RRID:SCR_000325
Python 3.10	Python.org	RRID:SCR_008394
Openmmlib	github.com/mirnylab/openmm-polymer-legacy	N/A
PyMol	pymol.org	RRID:SCR_000305
AlphaFold 3	alphafoldserver.com	RRID:SCR_025885
Deposited data		
Magnetic tweezers and AlphaFold analysis code	This paper[94]	Zenodo: https://doi.org/10.5281/zenodo.15036494
Single-molecule fluorescence data analysis code	This paper[15,95]	Zenodo: https://doi.org/10.5281/zenodo.10420524
Example single-molecule fluorescence data	This paper[93]	Zenodo: https://doi.org/10.5281/zenodo.16710550

EXPERIMENTAL MODEL AND STUDY PARTICIPANT DETAILS

Cloning procedures were carried out in *Escherichia coli* DH5α. Bacmids were generated in *E. coli* DH10EmBacY as described.[96] *E. coli* strains were grown at 37° C in LB (prepared in-house).

Spodoptera frugiperda Sf9 cells derived from pupal ovarian tissue of the female fall armyworm (Thermo Fisher Scientific; B82501) were cultured at 100 rpm and 27 °C in Grace medium (prepared in-house) supplemented with 10% fetal calf serum (Gibco; A5256801), 2 mM L-glutamine (Gibco; 25030-024), 1x Penicillin-Streptomycin (Sigma-Aldrich; P0781) and 0.1% Poloxamer 188 (Gibco; 24040-032).

For baculovirus infection of Sf9 cells, 1x10^6 Sf9 cells were seeded on a 6 well plate in 3 ml Sf-900 SFM media (ThermoFisher Scientific; 12658027), transfected with bacmid DNA using Fugene 6 (Promega) and incubated for 96 hours at 27 °C. The baculovirus-containing cell supernatant (V0) was then collected and used to infect 50 ml Sf9 cells at a density of 1 x10^6 cells/ml in Grace medium supplemented as described above. Cells were grown at 100 rpm and 27 °C, centrifuged 72 hours after infection and 9 ml cell supernatant (V1) was then used to infect 750 ml Sf9 cells at a density of 1.2 x10^6 cells/ml in Grace medium supplemented as above. Between one and four 750 ml cultures were infected per construct, depending on the predicted yield of recombinant protein. Cells were centrifuged around 54 hours after infection, washed in PBS, frozen in liquid nitrogen and stored at -80 °C.

METHOD DETAILS

Human cohesin, NIPBL-Mau2, STAG1, and NIPBL-ΔN expression and purification

Wild-type human cohesin, NIPBL-Mau2, and STAG1 were expressed in and purified from *Sf9* insect cells as described previously.[3,96] All steps were carried out at 4°C unless stated otherwise. *Sf9* insect cell pellets containing cohesin or NIPBL-Mau2, respectively, were subjected to Dounce homogenization in recombinant cohesin purification buffer 1 (25 mM NaH2PO4/Na2HPO4, pH 7.5; 500 mM NaCl; 5% glycerol) containing 10 mM imidazole, pH 7.5, 0.05% Tween 20, 1 mM PMSF, 3 mM beta-mercaptoethanol, 10 μg/ml aprotinin, 2 mM benzamidine, and cOmplete EDTA-free protease inhibitor cocktail. The lysate was clarified by centrifugation at 48,000 g for 45 minutes, and the resulting supernatant was incubated with 5 ml of Ni2+-charged Toyopearl AF-chelate-650M resin for 3 hours. Three successive washes were performed using 10 bead volumes of recombinant cohesin purification buffer 1 containing 15 mM imidazole, pH 7.5, and 0.01% Tween 20. Elution was achieved using 25 ml of recombinant cohesin purification buffer 2

(25 mM NaH2PO4/Na2HPO4, pH 7.5; 150 mM NaCl; 5% glycerol; 300 mM imidazole, pH 7.5; 0.01% Tween 20). The eluted material was then incubated with 5 ml of FLAG-M2 agarose resin for 3 hours, followed by 3 washes of 10 bead volumes each with cohesin purification buffer 3 (25 mM NaH2PO4/Na2HPO4, pH 7.5; 150 mM NaCl; 5% glycerol; 50 mM imidazole, pH 7.5). Proteins were eluted with 25 ml of recombinant cohesin purification buffer 3 supplemented with 0.5 mg/ml 3xFLAG peptide. The eluted protein was concentrated to approximately 0.5 ml using Vivaspin 20 ultrafiltration units (100 kDa MWCO; Sartorius; VS2042), flash-frozen in liquid nitrogen, and stored at -80°C.

NIPBL-ΔN was expressed and purified as above except that before elution from FLAG-M2 agarose, FLAG-M2 agarose beads were resuspended to one bead volume in 25 mM NaH2PO4/Na2HPO4 pH 7.5, 150 mM NaCl, 5 % glycerol, 50 mM imidazole pH 7.5. NIPBL- ΔN was then split in half, and fluorescently labeled with Atto550 and JF646, respectively, as described previously.[65] Here's a rewritten version maintaining all methodological details:

Stock solutions of Janelia Fluor 646 SE and HaloTag Amine (O2) Ligand were prepared at 20 mM and 50 mM, respectively, in dimethylformamide (DMF). A 248.7 μl conjugation reaction was assembled by combining HaloTag Amine (O2) Ligand with JF646 SE in DMF under continuous stirring, followed by addition of 1.3 μl diisopropylethylamine to achieve final concentrations of 7 mM JF646 SE, 2.3 mM HaloTag ligand, and 31 mM diisopropylethylamine. The reaction proceeded at room temperature for ∼16 hours in the dark. Following a 10-fold dilution in solvent A (5% acetonitrile, 0.1% formic acid), the product was purified through five consecutive reverse phase HPLC runs on an Ultimate 3000 system fitted with a Kinetex 5μ XB-C18 100A, 250 x 4.6mm column. The mobile phase consisted of solvent A (5% acetonitrile, 0.1% formic acid) and solvent B (acetonitrile, 0.1% formic acid), with a linear gradient from 0 to 100% B over 30 min at 0.8 ml/min. Collected peak fractions were combined, subjected to lyophilization, redissolved in DMSO, flash-frozen in liquid nitrogen, and maintained at -80°C. Protein fractions were incubated with purified HaloTag protein for 15 min at room temperature, followed by SDS-PAGE analysis and visualization using a Bio-Rad ChemiDoc MP.

For Atto550-HaloTag ligand synthesis, Atto550 NHS-ester was dissolved at 20 mM in dimethylformamide (DMF). A 245 μl conjugation reaction was prepared by combining HaloTag Amine (O2) Ligand with Atto550 NHS-ester in DMF under stirring conditions, followed by supplementation with 5 μl diisopropylethylamine to yield final concentrations of 25 mM Atto550 NHS-ester, 8.3 mM HaloTag ligand, and 115 mM diisopropylethylamine. The conjugation procedure followed the protocol established for Janelia Fluor 646 SE, with the modification that the crude reaction was diluted 10-fold in solvent A (40% acetonitrile, 0.1% Trifluoroacetic acid) and chromatographic separation employed a gradient of solvent A (40% acetonitrile, 0.1% Trifluoroacetic acid) to solvent B (acetonitrile, 0.1% Trifluoroacetic acid) from 0 to 100% B over 30 min at 0.8 ml/min.

For fluorescent labeling of recombinant NIPBL-ΔN with Atto550-HaloTag Ligand and JF646-HaloTag Ligand, the purification was divided into two equal portions. Each portion was treated with excess Atto550-HaloTag Ligand or JF646-HaloTag Ligand and allowed to react for 15 min at room temperature while shielded from light. Following extensive washing with recombinant cohesin purification buffer 3, protein elution and concentration were performed as above. Labeling efficiency determination yielded values of 86 ± 4% for NIPBL-ΔN-A550 (N = 7) and 85 ± 5% for NIPBL-ΔN-JF646 (N = 5).

As before,[65] protein and fluorophore concentrations were measured at 280 nm for NIPBL-ΔN and at 550/646 nm for A550/JF646, yielding a fraction of 86 ± 4 % labeled NIPBL-ΔN-A550 (N = 7) and 85 ± 5 % labeled NIPBL-ΔN-JF646 (N = 5) molecules. FCS was performed on samples of 10 nM NIPBL-ΔN-A550/JF646 in a buffer containing 40 mM Tris-HCl pH 7.5, 50 mM NaCl, 2.5 mM MgCl2, 1 mM DTT at room temperature. The resulting autocorrelation functions were well described by a fit with a single component, indicating that no free fluorophores were present.

Yeast condensin expression and purification

Wild-type yeast condensin was expressed and purified from *Saccharomyces cerevisiae* as described previously.[4] Typically, 0.5 l of preculture was grown on -URA-TRP medium supplemented with 2 g/l D-glucose (Merck Sigma G8270), six liters of main culture on -URA-TRP supplemented with 2 g/l D-raffinose (Biosynth R-1000), and condensin expression was induced with 2 g/l D-galactose (Biosynth G-1700). Cell lysates were prepared using a FreezerMill in buffer A (50 mM TRIS-HCl, pH 7.5; 200 mM NaCl; 5% glycerol; 5 mM β-mercaptoethanol; 20 mM imidazole) containing 1× cOmplete EDTA-free protease inhibitor mix. Following centrifugation to remove insoluble material, the clarified lysate was applied to a 5-mL HisTrap column, and bound protein was eluted using buffer A supplemented with 220 mM imidazole. The eluted fractions were treated with 1 mM EDTA, 0.2 mM PMSF, and 0.01% Tween-20, then subjected to overnight incubation with Strep-Tactin Superflow high capacity resin. Elution was performed using buffer B (50 mM TRIS-HCl, pH 7.5; 200 mM NaCl; 5% glycerol; 1 mM DTT) supplemented with 10 mM desthiobiotin. The resulting eluate underwent concentration via ultrafiltration, followed by size-exclusion chromatography on a Superose 6 column equilibrated in buffer B containing 1 mM MgCl2. Purified protein was flash-frozen and kept at –80°C.

Expression and purification of CTCF fragments

Various fragments of human CTCF (Uniprot #P49711, see Table S1) were cloned into a pMAL-C5X derived plasmid, resulting in MBP fusions with a flexible linker and a 3C protease site at the fusion point (MBP-NSSSNNNNNNNNNLGIEGRISHMSMGGRDIVDGSEF-LEVLFQ ↓GP-CTCF). Plasmids were transformed into *E. coli* ER2566 cells (New England Biolabs, fhuA2 lacZ::T7 gene1 [lon] ompT gal sulA11 R(mcr73::miniTn10–TetS)2 [dcm] R(zgb-210::Tn10–TetS) endA1 Δ(mcrCmrr)114::IS10) containing a Rosetta®-2 plasmid (Novagen), and selected on LB media containing 100 μg/ml ampicillin and 34 μg/ml chloramphenicol. For expression, overnight precultures were diluted 1:100 into 1 liter prewarmed LB with fresh antibiotics, cultures were grown in baffled flasks shaking at 200 rpm at

37°C until the OD600 reached ~0.6, and expression was induced by the addition of IPTG to a final concentration of 1 mM. After 3 hours of induction, the cells were harvested by centrifugation (8 min, 4500 rpm, JLA8.1000 rotor), washed in 50 ml PBS, and re-suspended in buffer A (50 mM Tris-HCl pH 7.5, 300 mM NaCl). Cells were lysed using a French Press (Constant Systems) at 20 kpsi, 4°C and unbroken cells, debris and aggregates were pelleted in a Ti45 rotor (30 min, 40.000 rpm, 4°C). The lysate was applied to 2 ml prewashed amylose resin (NEB #E8021) and incubated for one hour while rotating at 4°C. Subsequently, the resin was washed with 50 ml of buffer A and finally, CTCF fragments were eluted with 15 ml of buffer A supplemented with 1 mM β-mercaptoethanol and homemade 3C protease. CTCF fragments were concentrated using a Vivaspin centrifugal concentrator (10 kDa cut-off) and further purified by size exclusion chromatography (SEC) on a Superdex 200 Increase 10/300 column pre-equilibrated with buffer B (50 mM Tris-HCl pH 7.5, 150 mM NaCl, 5% (w/v) glycerol, 0.05 mM TCEP).

To purify the CTCF CTR (10xHis-CTCF(578-727)-TEV-Halo) and NTR^{ADA} (10xHis-CTCF(2-259)-TEV-Halo), baculovirus-infected insect *Sf9* cell pellets from cultures supplemented with 0.1 mM $ZnCl_2$ were lysed by Dounce homogenisation and resuspended in CTCF buffer (35 mM Hepes pH 7.5, 350 mM NaCl, 5% glycerol) supplemented with 0.1 mM $ZnCl_2$, 0.05% Tween-20, 5 mM imidazole, 1 mM PMSF, EDTA-free cOmplete tablet (1 per 50 ml) (Roche, 11873580001), 3 mM betamercaptoethanol, 10 μg/ml aprotinin, 2 mM benzamidine and benzonase. The lysate was cleared by centrifugation at 18,000 g for 45 min at 4°C. The soluble fraction was incubated with NiNTA agarose (Qiagen, 30230) for 90 min at 4°C and washed first with CTCF buffer supplemented with 0.1 mM $ZnCl_2$, 0.01 % Tween-20, 35 mM imidazole, 1 mM PMSF and 2 mM benzamidine and then with CTCF buffer supplemented with 35 mM imidazole only. Protein was eluted with CTCF buffer supplemented with 300 mM imidazole. The eluate was concentrated using a Vivaspin 30 kDa MWCO concentrator (Sartorius) and buffer was exchanged using a Zeba 7 kDa MWCO desalting column equilibrated in CTCF buffer. Protein was then flash-frozen and stored at -80°C.

In addition to these longer protein fragments, smaller fragments were synthesised in-house or ordered from Genscript (Table S1). Peptides were synthesised on a Liberty Blue peptide synthesiser (CEM) using standard Fmoc chemistry. For each amino acid cycle, a 4 min coupling with DIC/Oxyma was performed. Peptides were purified on a Phenomenex Luna C18(2) using a 2-45% in 45 min 0,1%TFA/ACN+0,1%TFA gradient. The identity of the peptide was confirmed using MALDI-MS (4800 MALDI TOF/TOF, Sciex)

Expression and purification of Scc1 fragment

A codon optimized gene for residues 252-420 of the human cohesin kleisin subunit (Uniprot O60216) was synthesized with a 3C protease site, an N-terminal cysteine and a C329S mutation, and cloned into the BamHI and EcoRI sites of pGEX-6P-1. The resulting plasmid pED145 was transformed into Escherichia coli ER2566 cells (New England Biolabs, fhuA2 lacZ::T7 gene1 [lon] ompT gal sulA11 R(mcr73::miniTn10–TetS)2 [dcm] R(zgb-210::Tn10–TetS) endA1 Δ(mcrCmrr)114::IS10) containing a Rosetta™-2 plasmid (Novagen), and selected on LB media containing 100 mg/ml ampicillin and 34 mg/ml chloramphenicol. For expression, overnight pre-cultures were diluted 1:100 into 1 liter prewarmed LB with fresh antibiotics, cultures were grown in baffled flasks shaking at 200 rpm at 37°C until the OD_{600} reached ~0.6, and expression was induced by the addition of IPTG to a final concentration of 1 mM. After 3 hours of induction the cells were harvested by centrifugation (10 min, 4000 rpm, JLA8.1000 rotor), washed in 50 ml PBS, and resuspended in buffer A (50 mM Tris/HCl pH 7.5, 200 mM NaCl, 5% (w/v) glycerol, 0.05 mM TCEP). Cells were lysed using a French Press (Constant Systems) at 20 kpsi, 4°C and unbroken cells, debris and aggregates were pelleted in a Ti45 rotor (30 min, 40.000 rpm, 4°C). The lysate was applied to 2 ml prewashed glutathione resin (Thermo Fisher 25237) and incubated for one hour while rotating at 4°C. Subsequently, the resin was washed with 50 ml of buffer A and finally the kleisin fragment was eluted in 15 ml of buffer A supplemented with homemade 3C protease. The kleisin fragment was concentrated using a Vivaspin centrifugal concentrator (10 kDa cut-off), fluorescently labelled with Alexa Fluor™ 647 C2 Maleimide (Thermo Fisher A20347) and further purified by size exclusion chromatography (SEC) on a Superdex 200 Increase 10/300 column pre-equilibrated with buffer A.

Synthesis of dsDNA construct for fluorescence-based loop extrusion experiments

The synthesis of the dsDNA construct based on λ phage DNA was described previously.[4] λ-DNA containing a biotin on both ends, was made by hybridizing and ligating short oligonucleotides containing 5′ phosphate and 3′ Biotin on the single-stranded DNA ends of Lambda DNA (NEB, N3011S). For this we used oligonucleotides, JT41 (P-GGGCGGCGACCT-Bio) and JT42 (P-AGGTCGCCGCCC-Bio) (IDT). Taq DNA ligase (NEB, M0208L) was used to ligate the oligonucleotide on Lambda, using 10 times molar access of oligonucleotide to Lambda DNA. The mixture was incubated for 10′ at 65°C and then 1hour at 50°C in Taq DNA ligase buffer. The biotin-Lambda DNA was then cleaned up from free oligonucleotides and enzymes using an AKTA pure system (Cytiva), with a homemade gel filtration column containing approximately 46 mL of Sephacryl S-1000 SF gel filtration media (Cytiva), run with TE + 150mM NaCl buffer at 0.2 mL/min. The fractions containing the Biotin-Lambda DNA were aliquoted and stored at −20 °C.

Synthesis of dsDNA construct for magnetic tweezers loop extrusion experiments

Singly biotinylated, linear dsDNA constructs with a length of 1.5 kbp were synthesised via PCR and enzymatically ligated to digoxigenin-enriched DNA handles, as described previously.[4] Briefly, a biotinylated DNA fragment of 1.5 kbp length was produced by using biotin-labeled forward and reverse primers that contain a BsaI restriction site on pBluescript II SK+. To create the digoxigenin-enriched handle, a 485 bp fragment from pBluescript II SK+ (Stratagene, Agilent Technologies Inc., USA) was amplified by PCR in the presence of 1:5 digoxigenin-11-dUTP:dTTP (Jena Bioscience, Germany). Prior to ligations of the DNA fragment and handle, the amplicons were digested with the non-palindromic restriction enzyme BsaI-HFv2 (New England Biolabs, UK). The ligation of the

DIG-handle and biotinylated DNA fragment was carried out overnight using T4 DNA ligase (New England Biolabs, UK). The final dsDNA construct was cleaned up from the access of handle by running on a 1% agarose gel and extracting the dsDNA construct using a gel purification kit (A9282, Promega) and stored at -20°C until use.

ATPase assay

20 nM recombinant human cohesin tetramer, 50 nM recombinant human NIPBL-Mau2, and 10 ng/μl λ-DNA were incubated in ATPase reaction buffer (final composition: 25 mM NaH_2PO_4/Na_2HPO_4 pH 7.5, 50 mM NaCl, 2.5 mM $MgCl_2$, 1 mM DTT, 0.1 mg/ml BSA, 2 mM ATP, and 10 nM $[\gamma\text{-}^{32}P]$ATP (Hartmann Analytic; SRP-501) at 37°C. Reactions were stopped by adding 1% SDS and 10 mM EDTA in a 10 min interval with 40 min endpoint. Where indicated, reactions were supplemented with CTCF peptide (freshly dissolved in 50 mM NaH_2PO_4/Na_2HPO_4 pH 7.5, 100 mM NaCl, 5% glycerol). Reaction products were separated on polyethyleneimide plates (Sigma; 1055790001) by thin-layer-chromatography using 0.75 M KH_2PO_4 (pH 3.4), analysed by phosphor imaging with a Typhoon Scanner (GE Healthcare), and quantified using ImageJ. The measured ATPase rates were normalised to the ATPase rate of cohesin in absence of CTCF fragments of the respective experiment day.

Synthesis of 5(6)-Carboxyfluoresceine-labeled KTYQR peptide

Peptide was synthesized on a Liberty Blue peptide synthesizer (CEM) using standard Fmoc chemistry. For each amino acid cycle, 4 min coupling with DIC/Oxyma was performed. N-terminal 5(6)-Carboxyfluoresceine was added under the same conditions as an amino acid. Peptide was purified on a Phenomenex Luna C18(2) using a 2-45% in 45 min 0,1%TFA/ACN+0,1%TFA gradient. The identity of the peptide was confirmed using MALDI-MS (4800 MALDI TOF/TOF, Sciex)

Single-molecule DNA loop extrusion assays

LE experiments and imaging were performed as described previously.[65] LE reactions by human cohesin were carried out in a buffer containing 40 mM Tris-HCl pH 7.5, 30 mM NaCl, 2.5 mM $MgCl_2$, 2.5% D-glucose, 2 mM Trolox, 10 nM catalase, 18.75 nM glucose oxidase, 100 nM Sytox Orange, 0.5 mg/ml BSA, 1 mM DTT, 1 mM ATP with 100 pM cohesin and 200 pM NIPBL-Mau2 at 37°C. For experiments with NIPBL-ΔN-A550/JF646, 100 pM cohesin, 15 pM NIPBL-ΔN-A550, and 15 pM NIPBL-ΔN-JF646 was used with 25 nM Sytox Green instead of Sytox Orange. 2 μM peptide was added were indicated. All data were acquired using an exposure time of 200 ms for LE experiments without double-labeled NIPBL-ΔN and using an exposure time of 300 ms in experiments with double-labeled NIPBL-ΔN.

Measuring DNA loop extrusion activity and steps with magnetic tweezers

The magnetic tweezers instrument and experimental methodology used in this study was previously described in detail.[56,58] Bead x, y, z position tracking was achieved with a spatial resolution of ~2 nm.[56] The concentration of cohesin was 100 pM together with 250 pM NIPBL-Mau2; the varying concentrations of the different CTCF fragments that were additionally added are denoted within the results description and Figures. Experiments were conducted at 22.3°C in a buffer containing 40 mM Tris pH 7.5, 40 mM NaCl, 2.5 mM $MgCl_2$, 1 mM DTT, 1 mM ATP, 0.05% Tween-20, 0.25 mg/ml BSA. Experiments with yeast condensin were conducted with 1.5-2 nM condensin at 22.3°C in a buffer containing 40 mM Tris pH 7.5, 40 mM NaCl, 2.5 mM $MgCl_2$, 1 mM DTT, 1 mM ATP, 0.25 mg/ml BSA. Data was acquired for 12 min after protein flush-in and lowering the applied force from 7 pN to 0.3 pN.

Datasets were processed using custom-written Igor v6.37-based scripts, removing traces that showed surface-adhered magnetic beads, ruptured tethers, as well as tethers containing more than one dsDNA.[56,58] The bead Z-positions of all traces conducted at identical conditions were pooled and filtered to 1 Hz (moving average) for subsequent quantitative LE-step analysis.

Fluorescence correlation spectroscopy

Fluorophore diffusion measurements were conducted using version 1 coverslips on a Picoquant Microtime 200 microscope, operated with Symphotime software at room temperature. A 60x Olympus UPSLAPO 60XW water immersion objective (working distance: 280 μm, numerical aperture: 1.2) was used to focus 485 nm (used for experiments with Cy3-labeled dsDNA) and 530 nm lasers (used for experiments with 5(6)-Carboxyfluoresceine-labeled KTYQR peptide). Prior to the experiment, the molecular brightness of Atto488 or Atto550 fluorophore solutions was optimised by adjusting the objective's correction collar. Emission light was directed through a 50 μm pinhole, split by a dichroic mirror, and filtered using a 520/35 optical band pass filter (Semrock) and a 563/9 band pass filter (Chroma). Fluorescence emission was collected by single-photon avalanche-diode detectors (PD5CTC and PD1CTC, Micro Photon Devices, Bolzano).

To examine affinity changes of $STAG1^{Scc1}$ to DNA in dependence of the YDF peptide, 10 nM of a Cy3-labeled 40 bp dsDNA (3'-CGTAGTCGGAGATGCGATTTGCATACCACCAG CGTAGTCG-5'), 150 nM $Scc1^{251\text{-}420}$, 15 nM STAG1, and the indicated excess of YDF peptide over STAG1 were incubated in a buffer containing 10 mM HEPES pH 7.5, 25 mM NaCl and 2.5 mM $MgCl_2$ for 30 min at room temperature. $Scc1^{251\text{-}420}$ was omitted where indicated and an equal volume of $Scc1^{251\text{-}420}$ storage buffer was added instead. ADA peptide was used instead of YDF peptide where indicated. To examine binding of 5(6)-Carboxyfluoresceine-labeled KTYQR peptide to STAG1, increasing concentrations of STAG1 were incubated with 20 nM labeled KTYQR peptide in a buffer containing 10 mM HEPES pH 7.5, 25 mM NaCl and 2.5 mM $MgCl_2$ for 30 min at room temperature.

AlphaFold predictions and structure analyses

Structure predictions of cohesin subunits and CTCF fragments were performed with AlphaFold v2,[72,73] downloaded from https://github.com/google-deepmind/alphafold. We used the default parameters except that all models were relaxed with a maximum number of 20 outer and 200 inner iterations. The sequences of the individual cohesin and CTCF fragments are listed in Table S2 and the individual chains as input to the AlphaFold-multimer pipeline are listed in Table S3.

3D polymer simulations

3D polymer simulations were performed as described by Banigan et al.,[69] with small modifications. A genomic region comprising 5600 monomers (1 monomer = 2 kb) was simulated containing 8 repeating elements of TADs spanning 400, 100, and 200 monomers respectively. These 8 elements were averaged to generate the contact maps shown in Figures S4F–S4H. Loop extruders switched their extrusion side and extruders underwent diffusion and slipping phases according to the experimentally observed rates.[65] When extruders encountered a barrier (CTCF), extruders stopped with the *stall probability*. If stalled, extruders stalled on both sides with the *probability to stall symmetrically*, i.e. extruders were not allowed to switch extrusion directions anymore and extrude away from CTCF. Additionally, extruders either could or could not be stalled by CTCF during diffusion and slipping phases.

In brief, 1D simulations were carried out by modeling each event as a Poisson process. At each LEF time step dt, an event is executed with probability $k_i dt$, where k_i is the rate of event i. 3D polymer simulations were subsequently performed using molecular dynamics in OpenMM[97,98] utilizing the openmm-polymer library (https://github.com/mirnylab/openmm-polymer-legacy), integrated with fixed-time-step LEF simulations as described in Fudenberg et al.[70] and Goloborodko et al.[99] Within the polymer simulation framework, LEFs establish crosslinks between their occupied sites. Following each LEF dynamics time step, polymer configurations are advanced through Langevin dynamics for 200 time steps with dt = 80. Polymer chains comprise L sequential subunits connected via the pairwise bonding potential

$$U_b(r) = \frac{k}{2}(r - b)^2$$

where $r = r_i - r_j$ represents the displacement between monomers i and j, the spring constant $k = 2\,kT/\delta^2$, $\delta = 0.1$, and b denotes monomer diameter. LEF-crosslinked monomers are constrained by an identical bonding potential. Excluded volume interactions between monomers are represented by a weak repulsive potential:

$$U_{exc}(r) = \frac{\varepsilon_{exc}}{\varepsilon_m}\left(\frac{r}{r_m}\right)^{12}\left((r_\sigma r_m)^2 - 1\right) + \varepsilon_{exc},$$

valid for $r < \sigma$ where $\sigma = 1.05b$, $r_m = \sqrt{\frac{6}{7}}$, $\varepsilon_m = 46656/823543$, and $\varepsilon_{exc} = 1.5\,kT$.

Initial conditions for each simulation consist of a random walk conformation for the polymer and velocities drawn from a normal distribution to establish temperature T. Temperature maintenance at T is achieved through periodic velocity rescaling. Simulations were run on nodes with access to a NVIDIA Tesla V100S using DelftBlue DHPC.[100]

Simulations were run for the following combination of parameters, totaling 338 simulations:

- Stall probability = [0, 0.01, 0.05, 0.1, 0.5, 0.6, 0.65, 0.7, 0.75, 0.8, 0.85, 0.9, 0.95]
- Probability to stall symmetrically = [0, 0.01, 0.05, 0.1, 0.5, 0.6, 0.65, 0.7, 0.75, 0.8, 0.85, 0.9, 0.95]
- CTCF can stall during diffusion and slipping phases = [yes, no]

QUANTIFICATION AND STATISTICAL ANALYSIS

Quantification and segmentation of kymographs

Kymographs were quantified and segmented as described in Barth et al.[65] In brief, images were cropped and processed by a median filter with a window size of 5 frames and the background was subtracted using a Top-Hat filter of size 10 pixels. The intensity of the DNA loop is normalised to the intensity along the entire DNA molecule and multiplied by the known length of the DNA molecule (48.5 kbp). The DNA loop position was determined as the relative position of the loop from one end of the DNA. Segmentation of cohesin-mediated LE phases was performed semi-automatically under assistance of a change point detection algorithm that was subsequently manually curated since an entirely automatic segmentation was not robust and returns spurious results on some traces or on parts of traces. After filtering, the change point detection was performed using a window-based change point detection algorithm,[101] which were subsequently merged and classified based on the error estimation of the assay.[34,65] The direction of each LE and DNA loop slipping phase was subsequently annotated by subjecting the DNA loop position over time within each segment to a linear regression and classifying the segment as direction1/direction2 based on the slope of the linear fit. Note that the nomenclature of the direction is arbitrary. Here, the first direction to which the loop travels is called direction 1.

A LE trace was labeled as unidirectional if all LE phases in the trace pointed in the same direction and as bidirectional otherwise. The frequency of LE phases was computed by dividing the number of LE phases by the time between the start of the first and last LE

phase of every trace. The direction switching frequency was computed by dividing the number of direction switches by the time between the start of the first and last LE phases of every trace.

The displayed DNA loop size and position traces (Figure 1C) were filtered using a Savitzky–Golay filter with a window length of 51 frames (5.1 s) and order 1 (implemented as part of the *scipy* package[102]).

To analyse the relationship between NIPBL-ΔN exchange and cohesin's extrusion direction switching, we monitored instances where the fluorescence intensity of one label was replaced by another, or where the intensity of one label disappeared and reappeared at least two frames later. The intensity of NIPBL-ΔN-A550/JF646 was calculated as the average intensity in the respective channel at the loop position, using a 5-pixel window around the loop centroid. Background intensity was subtracted by averaging the intensity in a region adjacent to the cropped DNA molecule, free from non-specific fluorescently labeled molecules during the loop lifetime.

We determined the number of bleaching steps by plotting the fluorescence intensity at the loop over time and counting the stepwise decreases to the background level, assisted by a hidden Markov model (HMM) analysis.[103] Only NIPBL-ΔN complexes associated with a DNA loop were considered. The NIPBL-ΔN residence time (Figure S3C) was calculated as the interval between the disappearance and preceding appearance of a NIPBL-ΔN molecule.

To correlate NIPBL-ΔN exchanges with extrusion direction changes, we counted direction changes during periods when NIPBL-ΔN dissociated from cohesin. Conversely, we also calculated the fraction of events where a direction change occurred concomitantly with a NIPBL exchange (Figures 2F and 2G).

Analysis of magnetic tweezers traces

The step-finding procedure is based on the quantitative method described by Smith in 1998 for detecting edges in noisy time-series data.[104] The algorithm was first made accessible for utilisation in the Python programming environment within the framework of the stepfinder Python package developed for the identification of steps in one-dimensional data with low signal-to-noise ratio[105] and subsequently refined to suit the specific requirements of single-molecule force spectroscopy experiments.

In brief, the algorithm enables the identification of steps with consistent reliability despite variable noise levels in the data as follows: at each time point x_i, the difference between the forward and backward estimation $\Delta_i = X_{i+} - X_{i-}$ of a Chung-Kennedy filter[106] applied to the time-series data is compared to the local root-mean-square (RMS) noise, calculated from the weighted moving variances $w_{i\pm} s_{i\pm}$ over the same window:

$$Y_i \frac{\Delta_i}{\sqrt{w_{i+} s_{i+} + w_{i-} s_{i-}}},$$

where the weights w correspond to the normalised switching factors of the Chung-Kennedy filter and are defined as

$$w_{i\pm} = \frac{s_{i\pm}^{-p}}{s_{i\pm}^{-p} + s_{i-}^{-p}},$$

with p being the nonlinearity factor (edginess) proposed by Chung and Kennedy. In practice, $p = 20$ was chosen. The quantity Y_i is also colloquially referred to as the *step score*, reflecting its role as a dimensionless indicator of step strength relative to the local noise level.

The noise component in the denominator is a function of the experimental conditions, e.g. magnetic tweezer force and DNA length. It consists of the weighted moving variance calculated to the mean of the data and averaged over a window and does not exhibit peaks at step locations, unlike the standard deviation. When an edge is encountered in the data, the output function Y responds with a triangular waveform peaking at the location of the edge itself.

The benefit of this edge detector is that its probability distribution is known, allowing for the calculation of confidence limits for the presence and absence of a step at each time point.[104]

This relationship is leveraged to define an initial threshold for the detection of a peak in Y

$$y_c = \frac{2}{3} \cdot \frac{\text{minimum step size}}{\text{local noise}} \qquad \text{(Equation 1)}$$

which ensures that the probability P_T for the detection of a true step (efficiency) is maintained at a constant level.

It can be shown that assuming an SNR of 1 and thus choosing $y_c = 2/3$ leads to the detection of steps with an efficacy (true positive rate) of 95%.

In addition, a downstream rejection procedure was applied to verify whether Equation 1 is satisfied for each detected individual step. For this purpose, the local step noise was computed within an interval around the index of the event, which was determined by the minimum allowed step spacing corresponding to two times the filter window. Based on this noise component and y_c, a dynamically adapting acceptance threshold value (in units of the input signal), for the current slice of the time trace was back-calculated corresponding to the minimum allowed step size in Equation 1. Above-threshold step sizes were considered valid, while below-threshold step sizes were rejected and the neighboring plateaus were merged. After each rejection, the quality of the remaining events was reassessed in an iterative procedure until the stepfinder output consisted of valid steps only (Figures S1C and S1D). To address the

fact that statistical predictors such as the probability of true and false outputs and localization accuracy of the stepfinder are also a function of the filter window width W, the algorithm systematically evaluated a sequence of 50 window sizes ranging from 0.5 s to 5.0 s. The final filter window size was selected by identifying the window width Wopt that minimized the standard deviation σ_{bkg} of step scores Y_i in putative non-step (i.e., below-threshold) regions. This criterion reflects the assumption that a narrow background score distribution indicates optimal separation between true steps and noise. To ensure robust step detection and avoid overfitting, the final window used for analysis was conservatively set to $\frac{4}{5} W_{opt}$. To further evaluate the suitability of each candidate filter window, the step scores Y_i of all accepted steps were again normalized by the standard deviation of background scores σ_{bkg} (i.e., the same value minimized during the window optimization). This yielded an apparent signal-to-noise ratio for each step, $SNR_i = Y_i/\sigma_{bkg}$, which quantifies the prominence of a detected step relative to the variability of background (non-step) scores. The mean and median of these individual SNR values were computed for each window size and served as additional metrics of step detection quality. While not directly used in the optimization, they typically approach their maximum near the window width that minimizes the background score variability, thereby supporting the choice of W_{opt} as the filter setting that best separates steps from noise.

This procedure, named *LowForceAutoStepfinder* (LFAS) was evaluated against a previously employed method to identify steps in MT traces of SMC-mediated LE (*AutoStepfinder*).[56] To this end, we computed the true positive rate (TPR) of detected steps using step validation data as conducted previously.[56] In brief, 1.5 kbp-long dsDNA was tethered between the glass surface and magnetic bead as described above and a force of 0.3 pN or 1 pN was applied. The piezo holding the objective was set to step up or down every 10 seconds for a range of step sizes (Figures S1E and S1F). Both stepfinder algorithms were applied to these traces. These datasets were then compared to the known steps from the piezo motion. In line with the previous stepfinder evaluation,[56] a step detection was judged correct if there was a piezo step nearby within 10% (~1 s) of the expected dwell time and 30% of the expected step size. We found that the LFAS has a higher TPR at smaller forces (in particular at 0.3 pN used in this study) and smaller induced step size (Figure S1G) and was thus used throughout this study.

Fitting of activity reduction and reversal/consecutive step ratio data

To fit the activity reduction in dependence of the peptide concentrations from MT experiments, the correlation between the peptide concentrations and the activity reduction data was first assessed using Spearman's correlation coefficient (function *scipy.stats.spearmanr* of the *scipy* package[102]). If the correlation coefficient was below 0.8, the data points were not subject to a fit, but described by a horizontal line with a height equal to the average value of the data points and the error bar equals the ± SD of the data points (e.g. CTR and NTR+condensin data in Figure 1M). When the Spearman's correlation coefficient exceeded 0.8, a piecewise linear model was fitted to the data that consisted of a horizontal line up to a concentration x_0 and a line with a negative slope thereafter in logarithmic space (e.g. NTR data in Figure 1I), i.e.

$$\begin{cases} B \text{ if } x \leq x_0 \\ B - m \log(x/x_0) \text{ if } x > x_0 \end{cases}$$

where B is an offset, m denotes the slope of the line in logarithmic space, and x_0 denotes the concentrations at which the horizontal line transitions into the line with a negative slope.

To fit the ratio of reversal to consecutive steps in dependence of peptide concentrations, the same approach was used, but the data points were fitted to the following function if the Spearman's correlation coefficient exceeded 0.8 (e.g. YDF data in Figure 2K):

$$y(x) = B + \frac{L}{1+(x/x_0)^{-1/k}}$$

This function is a logistic function with x and x_0 on a logarithmic scale. $L + B$ denotes the supremum of the function, and k is the logistic growth rate.

To provide a simple and robust description of the observed increase in reversals and the decrease in consecutive steps as a function of peptide concentrations, an exponential model was applied if, again, the Spearman's correlation coefficient exceeded 0.8:

$$y(x) = A \cdot exp(-kx) + B$$

where the amplitude A indicates the magnitude of change, and k is the convergence rate describing how quickly the system approaches its asymptotic value B, which represents either a maximum (for $A < 0$) or a baseline (for $A > 0$).

Analysis of FCS data

For fitting of the FCS curves (using PAM[107]), the size of the confocal volume was determined from measurements of the free dye by fitting a single-component diffusion model with triplet state (a diffusion constant of 297 $\mu m^2/s$ was used[108]). The axial and lateral sizes of the confocal volume were fixed for further analysis.

FCS curves of Cy3-labeled dsDNA binding to STAG1 were fitted with a single-component diffusion model with triplet state. The resulting diffusion constant was in good agreement with the theoretical diffusion constant of freely diffusing DNA (MW 26 kDa) and of dsDNA in complex with STAG1, $Scc1^{251-420}$, and YDF peptide (combined MW 182 kDa). Because the diffusion constant between the free and bound DNA differs only by a factor ~2, a two-component diffusion model with triplet state was overfitting the data.

The EC_{50} values of STAG1 - ± Scc1 - DNA data was estimated by converting the measured diffusion constants to the bound fraction of DNA by normalizing between the diffusion constant of unbound and STAG1-Scc1-bound DNA, respectively. Then, a non-linear regression of the data to the Hill equation, $DNA_{bound} = [x]^n/(K_A{}^n + [x]^n)$, where [x] is the excess of peptide over STAG1, was performed to estimate the K_A value which, here, equals EC_{50}.

FCS curves of 5(6)-Carboxyfluoresceine-labeled KTYQR peptide were fitted with a two-component diffusion model with triplet state with fixed diffusion constants of the free peptide (MW 2 kDa) and the KTYQR peptide in complex with STAG1 (combined MW 139 kDa). The relative amplitude of the bound and unbound fraction is shown in Figure 3K.

Conservation score annotation

Conservation scores were computed using the ConSurf webserver (consurf.tau.ac.il).[109,110]

AlphaFold structure predictions analyses

After the structure prediction, individual predictions of a combination of cohesin subunits and CTCF fragments were aligned on the NIPBL, STAG1, STAG2, or Smc3, respectively, using custom scripts using *PyMOL*.[111] The structures were also rendered in PyMOL. The structural similarity of individual amino acids within CTCF fragments #1-3 (and scrambles thereof) was computed as follows: the C α coordinates were extracted from the PDB files and the distance of each amino acid in prediction pi to the corresponding amino acid in prediction p_j was computed, where $i \neq j$. Subsequently, the median distance of each amino acid in the prediction p_i to all other predictions was computed and displayed as one individual line (the median distance of each amino acid in prediction p_i to all other predictions) in Figure S6C.

Analysis of 3D polymer simulations

From the resulting polymer configurations, contact maps and the contact frequency as a function of genomic distance *s* (P(s)) were computed from 4000 conformations using the openmmlib package (https://github.com/mirnylab/openmm-polymer-legacy) with a contact radius of 5 monomers. The simulated P(s) curves were quantitatively compared to experimental P(s) curves from wild-type Hap1 cells as reported by Haarhuis et al.[31] and the goodness of fit between simulated and experimental P(s) curves was computed as the geometric standard deviation of the ratio of simulated to experimental P(s) as before.[70] Each parameter combination was ranked by its goodness of fit either for a fixed combination of the stall probability and whether CTCF can stall cohesin during diffusion and slipping phases (Figures S4B and S4C) or overall (Figures S4D and S4E). Similarly, we computed the colocalization of CTCF and SMC1 in experimentally obtained ChiP-seq data from Haarhuis et al.[31] which yielded that 41.5% of CTCF peaks colocalized with an SMC1 peak and 95.1% of the SMC1 peaks colocalized with a CTCF peak with a window of 2 kb, matching the simulated genomic resolution. The variability across chromosomes was 25% for CTCF and 50% for SMC1. Similarly, we computed the colocalization percentages across simulation parameters, where we used only the "leg" of the SMC closer to any CTCF to mimic the SMC1 ChiP-seq experiment. We used these values to rank simulation parameters (Figures S4J and S4K) by computing their Mahalanobis distance, accounting for the fact that CTCF and SMC1 distributions are correlated due to the known fact that CTCF and cohesin interact, as well as for the different variance of colocalization percentages across chromosomes.

STATISTICAL ANALYSES

Statistical tests were performed using the *scipy* module[102] or using GraphPad Prism 9. Details of statistical test performed on the presented data are stated in the figure captions.